Lithospheric Structure of Africa and Surrounding Regions Revealed by Earthquake and Ambient Noise Surface Wave Tomography

Adebayo Oluwaseun Ojo[1], Weisen Shen[2], Sidao Ni[3], Li Zhao[4], Jun Xie[5], and Honn Kao[6]

[1]Geological Survey of Canada, Natural Resources Canada
[2]Stony Brook University
[3]CAS Institute of Geodesy and Geophysics
[4]Peking University
[5]Innovation Academy for Precision Measurement Science and Technology, Chinese Academy of Sciences
[6]Geological Survey of Canada

November 26, 2022

Abstract

To advance the understanding of the tectonic processes shaping the African continent, we construct the first continental-scale shear-wave velocity (Vs) model of the crust and uppermost mantle from joint analysis of ambient seismic noise and earthquake data recorded by ~1529 broadband seismic stations located in Africa, Arabia, and Europe from 1987 to 2018. We apply the widely used ambient noise cross-correlation and earthquake two-station methods to retrieve the fundamental-mode Rayleigh-wave group and phase velocity dispersions in the period range of $5 - 50$ s which are jointly inverted using the neighbourhood algorithm to build a new three-dimensional Vs model with associated uncertainties. The inclusion of relatively short-period dispersion data from ambient seismic noise allows us to achieve better resolution at shallow depth and obtain a more accurate model than previous global and continental-scale studies, revealing lithospheric structures that correlate well with known tectonic features. In sparsely instrumented regions of north-central Africa, our model provides seismic evidence for the existence of cratonic remnants beneath thick sediments within the poorly imaged Sahara Metacraton and reveals unique mantle upwelling beneath hotspots, suggesting that they may be fed by unconnected plumes. The estimated crustal thickness varies among and within tectonic provinces and shows no clear evidence for the secular variation in crustal genesis. Our new model has the potential to serve as a preliminary reference velocity model for Africa and is useful for practical applications, including monitoring of the Comprehensive Nuclear-Test-Ban Treaty, geodynamic modeling as well as seismic hazard analysis.

Lithospheric Structure of Africa and Surrounding Regions Revealed by Earthquake and Ambient Noise Surface Wave Tomography

Adebayo Oluwaseun Ojo[1,4], Weisen Shen[2], Sidao Ni[3], Li Zhao[1], Jun Xie[3], Honn Kao[4,5]

[1]School of Earth and Space Sciences, Peking University, Beijing, 100871, China
[2]Department of Geosciences, State University of New York at Stony Brook, Stony Brook, NY, USA
[3]State Key Laboratory of Geodesy and Earth's Dynamics Institute of Geodesy and Geophysics, CAS
[4]Geological Survey of Canada, Natural Resources Canada, Sidney, British Columbia, Canada
[5]School of Earth and Ocean Science, University of Victoria, Victoria, British Columbia, Canada

Abstract

To advance the understanding of the tectonic processes shaping the African continent, we construct the first continental-scale shear-wave velocity (Vs) model of the crust and uppermost mantle from joint analysis of ambient seismic noise and earthquake data recorded by ~1529 broadband seismic stations located in Africa, Arabia, and Europe from 1987 to 2018. We apply the widely used ambient noise cross-correlation and earthquake two-station methods to retrieve the fundamental-mode Rayleigh-wave group and phase velocity dispersions in the period range of 5 – 50 s which are jointly inverted using the neighbourhood algorithm to build a new three-dimensional Vs model with associated uncertainties. The inclusion of relatively short-period dispersion data from ambient seismic noise allows us to achieve better resolution at shallow depth and obtain a more accurate model than previous global and continental-scale studies, revealing lithospheric structures that correlate well with known tectonic features. In sparsely instrumented regions of north-central Africa, our model provides seismic evidence for the existence of cratonic remnants beneath thick sediments within the poorly imaged Sahara Metacraton and reveals unique mantle upwelling beneath hotspots, suggesting that they may be fed by unconnected plumes. The estimated crustal thickness varies among and within tectonic provinces and shows no clear evidence for the secular variation in crustal genesis. Our new model has the potential to serve as a preliminary reference velocity model for Africa and is useful for practical applications, including monitoring of the Comprehensive Nuclear-Test-Ban Treaty, geodynamic modeling as well as seismic hazard analysis.

1 Introduction

The continent of Africa contains several important tectonic features with records that span well over 3.7 Ga of earth's history (Milesi et al., 2010). These include Archean Cratons, Proterozoic mobile belts, Mesozoic and Cenozoic rifts and hotspots, large sedimentary basins, and widespread Precambrian crust that have been shaped by several past and ongoing tectonic processes (Begg et al., 2009). Surrounding the continent are divergent plate boundaries and passive continental margins resulting from the Mesozoic breakup of Gondwana and the opening of the Atlantic Ocean (Ebinger, 2005; Fishwick & Bastow, 2011; Tugume et al., 2013; Figure 1). The scientific curiosity to understand the origin and evolution of these

36 prominent geological features in Africa led to the deployment of a growing number of seismic networks,

37 e.g., the Africa-Array (Durrheim, 2008; Nyblade et al. 2008; Durrheim & Nyblade, 2019), SASE (Yang et

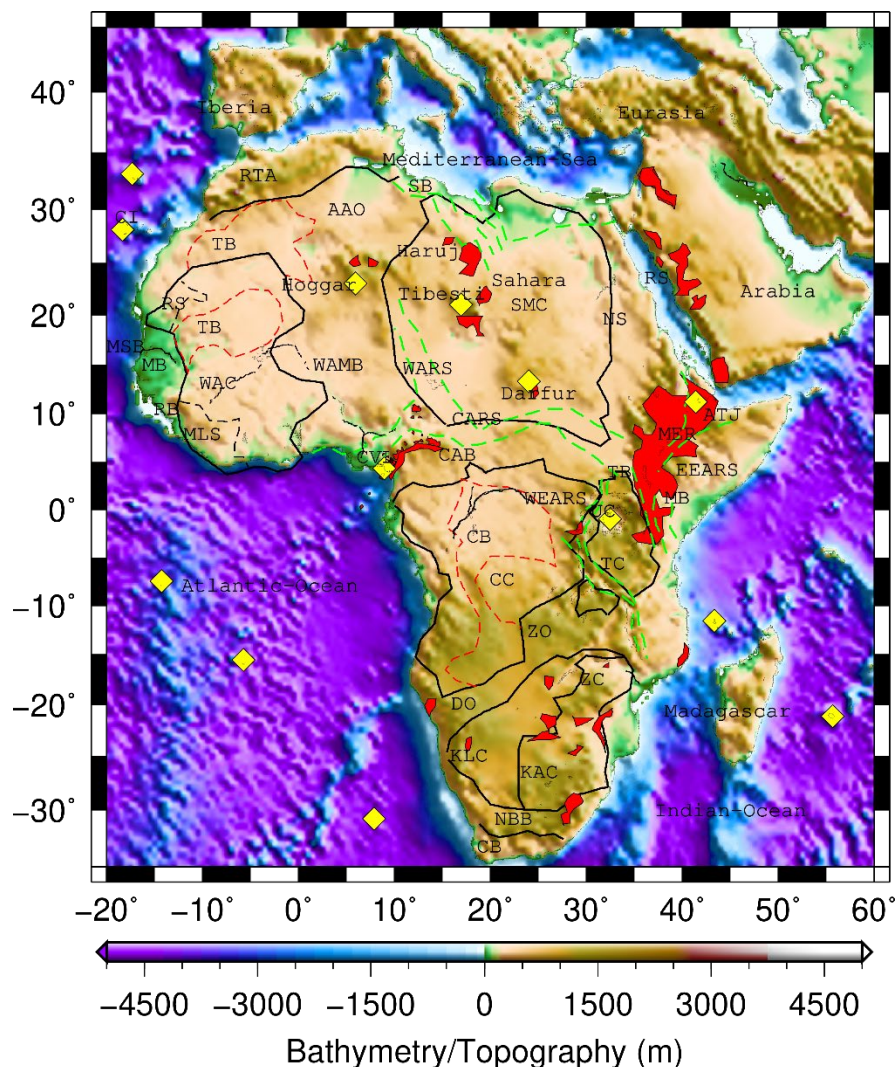38 al., 2008), CBSE (Tokam et al., 2010), etc. in and around the African continent in the past few decades.

39

40

41 **Figure 1.** Map of the study area showing the main tectonic features (modified after Globig et al., 2016)

42 overlain on the bathymetry and topography derived from ETOPO1 (Amante & Eakins, 2009). Denoted on

43 the map are the locations of the tectonic features in and around the African continent including CPB (Cape

44 Belt), NNB (Namaqual-Natal Belt), KLC (Kalahari Craton), KAC (Kaapvaal Craton), ZBC (Zimbabwe

45 Craton), DMO (Damara Orogen), ZBO (Zambezi Orogen), CGC (Congo Craton), CGB (Congo Basin),

46 TZC (Tanzania Craton), UGC (Uganda Craton), WEARS (Western East African Rift System), EEARS

47 (Eastern East African Rift System), TKB (Turkana Basin), MZB (Mozambique Belt), MER (Main

48 Ethiopian-Rift), ATJ (Afar Triple Junction), CVL (Cameroon Volcanic Line), CAB (Central African Belt),

2

49   CARS (Central African Rift System), WAC (West African Craton), WAMB (West African Mobile Belt),

50   NBS (Nubia Shield), RS (Red Sea), SRB (Sirt Basin), MLS (Man-Leo Shield), TDB (Taoudeni Basin),

51   RKB (Rockellides Belt), MTB (Mauritanian Belt), MSB (Mauritanian-Senegal Basin), RGS (Reguibat

52   Shield), CNI (Canary Island); RTA (Rif-Tell-Atlas Mountain); AAO (Anti-Atlas Orogen), SMC (Saharan

53   Metacraton). Red patches and yellow diamonds show locations of Cenozoic volcanism and hotspots,

54   respectively. Green dashed lines mark zones of continental rifting and red dashed lines define boundaries

55   of intra-cratonic basins.

56   Data from these deployments have been used in a lot of studies that provided us with a fundamental

57   understanding of the structure, composition, and geodynamic evolution of these tectonic features (e.g.,

58   Adams et al., 2018; Accardo et al., 2020; Celli et al., 2020; Chambers et al., 2019; Ebinger et al., 2019;

59   Hassan et al., 2020; Hopper et al., 2020; Kachingwe et al., 2015; Ojo et al., 2018, 2019; Sobh et al., 2020;

60   Wang et al., 2019 and references therein). However, these studies are either small-scale local or large-scale

61   global studies that do not sufficiently address the regional-scale lateral and depth variations of the

62   lithospheric structure of the entire African landmass. A cross-evaluation of the existing models from small-

63   scale studies across the continent published by different authors is not straightforward as they came from

64   different datasets with varying measurement uncertainties, non-uniform processing techniques, and

65   resolutions in addition to the use of a variety of methods. Our current understanding of the continental-scale

66   lithospheric structure of Africa and the relationship between the various tectonic provinces primarily came

67   from global models that cover this continent, however, they usually bear worse resolution and not capable

68   to address specific scientific problems of interest (e.g., Woodhouse & Dziewonski, 1984; Cadek &

69   Martinec, 1991; Trampert & Woodhouse, 1995; Nataf & Richard, 1996; Mooney et al., 1998; Ritsema et

70   al., 1999; Boschi & Ekstrom, 2002; Grand, 2002; Ritzwoller et al., 2002; Shapiro & Ritzwoller, 2002; Zhou

71   et al., 2006; Meier et al., 2007; Lebedev et al., 2009; Pasyanos et al., 2014; Rychert & Shearer, 2009; Laske

72   et al., 2013; Schaeffer & Lebedev, 2013). This is primarily attributed to a lack of data in several parts of

73   the continent inhibiting their ability to achieve a satisfactory resolution to targeted structures. The majority

74   of existing broadband seismic stations are located in the southern and eastern parts of the continent,

75   therefore, a good portion of the continent (e.g., Central, Northern and Western parts) remains poorly

76   constrained seismologically due to the lack of densely and uniformly distributed stations in addition to low

77   seismicity (Van der Meijde et al., 2015; Figure 2). To the best of our knowledge, only a limited number of

78   studies have attempted to develop a regional-scale model of Africa from seismic and/or gravity data (e.g.,

79   Sebai et al., 2006; Pasyanos & Nyblade, 2007; Priestley et al., 2008; Begg et al., 2009; Fishwick, 2010;

80   Tedla et al., 2011; Laske et al, 2013; Tugume et al., 2013; Pasyanos et al, 2014; Globig et al., 2016; Celli

81   et al., 2020). More so, these previous regional-scale studies on the continent focused more on the upper

82   mantle structure while ignoring or correcting for crustal effects, leaving fundamental questions regarding

3

83 the crustal structure unresolved (e.g., Deen et al., 2006; Ritsema & van Heijst, 2000; King & Ritsema, 2000;

84 Lekic et al., 2010; Panning et al., 2010; Beggs et al., 2009; Adams et al., 2012; Emry et al., 2019).

85 A more comprehensive understanding of the regional tectonics of Africa necessitates the development of a

86 robust continent-wide seismic model from detailed imaging of both shallow and deep structures across the

87 continent using the same methodology and data processing procedure. An effective approach to solving the

88 current situation of uneven data coverage and achieving this goal would be to densify the seismic stations

89 across the African continent as we have in other more developed parts of the world, such as the USArray

90 and Hi-net programs. However, this is an expensive approach with economic constraints and other

91 challenges. In this study, we adopt a proactive approach to mitigating this problem and develop a new

92 seismic model of the African lithosphere that provides significant improvements over previous continental-

93 scale studies. For the first time, we combine dispersion data obtained from cross-correlations of ambient

94 seismic noise and earthquake records to image the entire African continent similar to other successful

95 studies (e.g., Yao et al., 2008; Yang et al., 2008a,b; Yang & Ritzwoller, 2008; Lebedev et al., 2009;

96 Moschetti et al., 2010; Yoshizawa & Ekstrom, 2010; Endrun et al., 2011; Zhou et al., 2012; Agius &

97 Lebedev, 2013; Shen et al., 2013; Huang et al., 2014; Chen et al., 2014; Pourpoint et al., 2018; Ojo et al.,

98 2018). This enables us to obtain up to 50,000 inter-station ray paths crisscrossing the entire continent at an

99 unprecedented density, thereby improving the spatial resolution in sparsely instrumented regions in Africa

100 and achieve sensitivity to both shallow and relatively deep lithospheric structures (e.g., Kastle et al., 2018;

101 Pourpoint et al., 2018). This paper discusses this effort by first providing a summary of the tectonic settings

102 in the study area in Section 2, showing the data and method in Section 3, and then presenting the results

103 and interpretation in Section 4. We also provide a detailed discussion on specific scientific questions in

104 Section 5 and summarize the paper in Section 6.

105 **2. Tectonic and Geological Configuration of the Study Area**

106 In this section, we provide a sufficient description of the most remarkable geologic features in the Eastern,

107 Western, Southern, and Northern part of the continent as a guide to the interpretation of the shear-wave

108 velocity model developed in this study. However, we acknowledge that it is outside the scope of this paper

109 to present a detailed tectonic evolution of the African continent and refer readers to Begg et al. (2009) and

110 references therein for a more complete description of the African geology and tectonics.

111

112 **2.1 Eastern Africa**

113 The region of eastern Africa has been the attention of a lot of studies primarily because of the ongoing

114 continental rifting along the boundary between the Nubia and Somalia plates, marked by the 5000 km long

115 East African Rift System (EARS) which is active both seismically and volcanically (McConnell, 1972;

Chorowicz, 2005). This divergent plate boundary extends from eastern to southern Africa and preferentially splits into two distinct branches (i.e. the eastern EARS and the western EARS) in the center around the Archean Tanzania Craton (TZC, see Figure 1). Although the western EARS is seismically active and characterized by a few isolated regions of magmatism, the eastern EARS is characterized by widespread magmatism (Ebinger, 1989). The EARS exhibit different stages and styles of continental rift development that is most likely enhanced by magmatic processes in the upper mantle (e.g., Nyblade & Robinson, 1994; Bagley & Nyblade, 2013; Ring, 2004). Its geodynamic origin and evolution are hotly debated in literature with proposed mechanisms ranging from single to multiple plumes and possible connection to the African Superplume (e.g., Nyblade & Robinson, 1994; Grand et al., 1997; Ebinger & Sleep, 1998; George et al., 1998; Lithgow-Bertelloni and Silver, 1998; Ritsema et al., 1998, 1999; Gurnis et al., 2000; Rogers et al., 2000; Furman et al., 2004; Kieffer et al., 2004; Benoit et al., 2006; Pik et al., 2006; Simmons et al., 2007; Bastow et al., 2008; Forte et al., 2010; Hilton et al., 2011; Hansen & Nyblade, 2013).

The Red Sea and Gulf of Aden rifts began forming in the Oligocene when Arabia first separated from Africa. Together with the East African Rift, they form a triple junction in the Afar depression (Begg et al., 2009). The Main Ethiopian Rift (MER) is in the northern part of the EARS where magma-assisted continental rifting started about 31–29 Ma and transitions into incipient seafloor spreading in Afar depression (Wolfenden et al., 2004; Bosworth et al., 2005). The MER transects the Ethiopian Plateau, a 1000 km wide Palaeogene flood basalt province uplifted to an elevation of ~2.5 km after the impingement of the Afar mantle plume at the base of the lithosphere around ~30 Ma (Ebinger & Sleep, 1998). The magma-poor and weakly extended Malawi rift zone is about 800 km long beginning from the Rungwe Volcanic Province in the north to the Urema Graben in the south and mainly occupied by Lake Malawi which consists of several half-grabens bounded by border faults (e.g., Ebinger et al., 1989; Jackson & Blenkinsop, 1993; Craig et al., 2011; Fagereng, 2013; Laó-Dávila et al., 2015).

The Uganda and Tanzania Cratons are both located between the western and eastern branches of EARS. The Achaean TZC forms the nucleus of the Precambrian tectonic framework of eastern Africa and is surrounded by several Proterozoic mobile belts which are shaped primarily by the process of obduction (Cahen et al., 1984). The dominant rock types that make up the TZC are granitoid and gneisses formed about 2.7-2.5 Ga and the Palaeoproterozoic Rwenzori Fold Belt in the northwest consisting mainly of metasedimentary rocks intercalated by granitoid (Cahen et al., 1984; Schulter, 1997; Manya & Maboko, 2003; Begg et al., 2009). The Uganda Craton lies to the north of the TZC and contains Neoproterozoic units that overlie its northeastern boundary with the Congo Craton in southwestern Africa. During the last 80 Ma, the craton has been affected by kimberlite volcanism (Chesler, 2012).

2.2 Northern Africa

150 The northward movement of the relatively stable African continent (~2–6 mm/yr) and its subsequent
151 collision with the Eurasian plate starting from ~40 Ma led to the closure of the Tethys Ocean and the
152 formation of tectonically complex northern and northwestern margins of the African plate (e.g., Abdelsalam
153 et al., 2002, 2011). This also led to the formation, beginning from Cenozoic till today, of the Rif-Tell-Atlas
154 Orogenic system, an intra-continental mountain belt marked by high topography (~2000 m) extending over
155 2000 km from Morocco to Tunisia (see Figure 1). Although the geodynamic evolution of the Rif-Tell
156 Mountains of the Atlas System is highly debatable, it is suspected to result from the closure of the Tethys
157 Ocean by subduction in the Western Mediterranean and further slab retreat (e.g., Vergés & Sàbat, 1999;
158 Faccenna et al., 2004; Rosenbaum & Lister, 2004). The northward movement of the African plate and its
159 convergence with the Eurasian plate also complicates the geology of the Mediterranean region in southern
160 Europe (Faccenna et al., 2001; Lu et al., 2018; Manu-Marfo et al., 2019). The region is marked by
161 subductions and collision of several microplates sandwiched between the larger tectonic plates. Similarly,
162 several Triassic and Jurassic rifting episodes created basins (e.g., the Central African Rift System) along
163 the inherited zones of crustal weakness in combination with the opening of the Atlantic Ocean (e.g., Frizon
164 de Lamotte et al., 2000).

165 Eocene to Quaternary hotspot volcanic centers marked by topographic swells are also found in northern
166 Africa. They are Hoggar in southern Algeria, Tibesti in northern Chad, and Darfour in western Sudan
167 (Brown & Girdler, 1980; Nocquet & Calais, 2003; McClusky et al., 2003; Rosenbaum & Lister, 2004).
168 Investigations of the magmatic plumbing system beneath these alkaline volcanoes suggest the existence of
169 a unique plume source beneath all the volcanic centers or the migration of plumes from the Afar depression
170 (Wilson & Guiraud, 1992; Burke, 1996; Ebinger & Sleep, 1998). Additionally, the upwelling of plumes
171 due to small-scale mantle convection induced by the Africa-Eurasia collision may also be responsible for
172 feeding the volcanic centers (Bailey, 1992).

173 Also in northern Africa is the enigmatic Saharan Metacraton which underlies much of the Sahara desert
174 region between the West African Mobile Zone and the Arabian-Nubian Shield (Schandelmeier et al., 1994;
175 Abdelsalam et al., 2002). The pre-Neoproterozoic character of its cratonic fragments indicates that it has
176 been reworked by later Neoproterozoic collision events which most likely led to the delamination and/or
177 basal erosion of the cratonic lithosphere (Abdelsalam et al., 2002; Lucassen et al., 2008; Begg et al., 2009;
178 Shang et al., 2010; Fezaa et al., 2010; Abdelsalam et al., 2011). Likewise, the presence of scattered
179 Precambrian outcrops in the region possibly indicates the existence of cratonic bodies underneath the thick
180 Phanerozoic sediments in the Sahara desert (Condie, 1982).

181 Adjacent to the African plate in the northeast is the Arabian plate characterized by the Arabian shield
182 near the Red Sea and Arabian Platform towards the eastern part of the plate. The plate is covered by
183 sediments that thickens towards the east from the shield to the Mesopotamian Foredeep and Persian Gulf

184   (Seber et al., 1997; Tang et al., 2016; Yao et al., 2017; Kaviani et al., 2020). Expressions of widespread

185   Cenozoic volcanism are also found within the plate.

186

187   **2.3 Southern Africa**

188   The region of southern Africa is characterized by anomalously high elevations compared to the global

189   continental average elevation and contains the world's oldest Archean cratons (i.e. the Zimbabwe and

190   Kaapvaal cratons) sandwiched between Orogenic belts. It also hosts two renowned igneous provinces, the

191   Okavango dyke swarm and Bushveld mafic intrusion, formed between 2.7 and 0.3 Ga (de Wit et al., 1992;

192   Nyblade & Robinson, 1994; Jelsma & Dirks, 2002). The Kaapvaal craton combines several terranes which

193   consist mainly of granite-greenstone with narrow greenstone belts formed between 3.7 and 2.7 Ga and

194   subsequently affected by several tectono-thermal events (De Wit et al., 1992; Eglington & Armstrong,

195   2004; Johnson et al., 2006; Begg et al., 2009). Similarly, the Zimbabwe craton formed between 3.6 and 2.5

196   Ga. The craton is underlain by the Paleoarchean lithosphere, suggesting that the isolation from the

197   convective mantle most likely occurred during the initial phase of craton formation. The last tectono-

198   thermal event that affected the craton occurred during the emplacement of the Great Dike around 2.58 Ga

199   (Jelsma & Dirks, 2002). The Zimbabwe and Kaapvaal cratons are separated by the east-west trending

200   Limpopo orogenic belt resulted from the collision between the two cratons around 2.7 Ga. The Limpopo

201   orogenic belt consists of highly metamorphosed granite-greenstone and granulite terrains, which underwent

202   a series of orogenic events between 2.0 and 3.0 Ga (McCourt & Armstrong, 1998; Kramers et al., 2006).

203   Located in the southernmost end of the region is the Cape Fold Belt (0.3 Ga) formed during a younger

204   orogenic event in the late Proterozoic/early Cambrian Saldanian Orogeny and the late-Paleozoic Cape

205   Orogeny (Rozendaal et al., 1999). The youngest tectonic province in the region is the Namaqua-Natal

206   mobile belt which was joined with the Kaapvaal Craton during the Namaqua Orogeny between 1.3 and 1.0

207   Ga. A large proportion of the belt has been covered by Phanerozoic sediments with a few surface exposures

208   in the eastern Natal and the western Namaqua sectors (Thomas et al., 1989; Cornell et al., 2006).

209   Off the southeastern shore of Africa lies Madagascar that drifted south-southeasterly away from Africa

210   along with India about 165–130 Ma during the break-up of Gondwana (Rabinowitz et al., 1983; Coffin &

211   Rabinowitz, 1987; Kusky et al., 2007). This led to the opening of the Mozambique Channel and the

212   formation of the Somali and the Mozambique oceanic basins (Rabinowitz et al., 1983; Piqué, 1999).

213   Similarly, the rifting thinned the crust along the west coast of Madagascar, allowing Late Carboniferous to

214   Quaternary age sedimentary basins, such as the Antsiranana, Mahajanga, and Morondava rift basins, to

215   form on top of the Karoo sequence. This also led to the emplacement of volcanic rocks that have been

216   reworked during the Pan-African Orogeny across many regions of Madagascar (e.g. Rabinowitz et al.,

217   1983; Coffin & Rabinowitz, 1987; Nicollet, 1990; Storey et al., 1995; Torsvik et al., 1998; de Wit, 2003;

Collins, 2006; Pratt et al., 2017). The widespread flood basalts with surface exposure along the periphery of the island are commonly linked to the migration of Madagascar/India over the Marion hotspot (Storey et al., 1995; Torsvik et al., 1998). Subsequent rifting of the Indian subcontinent along a transform fault from 95 Ma to 84 Ma further shaped the east coast of Madagascar (e.g., Nicollet, 1990; de Wit, 2003). Since then, the entire island has remained tectonically stable.

2.4 Western Africa

The geology of western Africa is characterized by the Archean West African Craton (WAC) which contains a mechanically weak intra-cratonic depression in the center playing host to the Taoudeni Basin filled with ~3 km of Neoproterozoic to Paleozoic deposits alongside two other sedimentary basins, the Tindouf and Volta basins, and major shield bodies, the Reguibat and Man shields (MacGregor et al., 1998; Figure 1). Sedimentation in the basins began in late Proterozoic and continued well into Phanerozoic (Petters, 1991). Several Pan-African and Hercynian belts surround the WAC along the eastern (the Pharusian and Dahomeyides belts), western (the Rokellides and Mauritanides belts) and northern (Anti-Atlas belt) margins. The WAC and the Saharan Metacraton to the north are separated by the West African Mobile Zone (WAMZ), a typical configuration observed around Archean cratons in different parts of the continent. The Archean to Paleoproterozoic Congo Craton occupies most of the landmass in the southern part of western Africa and is surrounded by Pan-African foreland belts. The craton consists of granites and gneisses intruded by magmatic rocks that have been altered to form the greenstone belts which were subsequently intruded by granodiorites at about 2.9 Ga (Cahen et al., 1984; Tchameni et al., 2001; Begg et al., 2009; Tadjou et al., 2009). The craton also contains an intracontinental depression which is largely covered by the Proterozoic Congo Basin filled with about 4–9 km of Proterozoic to Neogene sediments with very slow subsidence since the Pan-African event (Crosby et al., 2010; Kadima et al., 2011). A large portion of western Africa experienced flood magmatism at about 137–127 Ma when the south Atlantic opened (e.g., Turner et al., 1994). The Mesozoic rifting and break-up of Gondwana led to the development of the Central African Rift System and the widespread extensional basins from Somalia to South Africa (e.g., Veevers et al., 1994; Burke, 1996).

The Cameroon Volcanic Line (CVL) is a linear chain of volcanoes of about 1600 km long traversing both the ocean (Gulf of Guinea) and the continent in Cameroon, western Africa. CVL comprises of 10-15 volcanic centers without age progression, a characteristic that makes it enigmatic. Volcanism commenced at 42 Ma in the continental sector and 30 Ma in the oceanic sector, and the volcanic rocks in both the oceanic and continental sectors are predominantly alkaline basalts (Fitton & Dunlop, 1985). The origin of the Eocene to Recent alkaline volcanoes is mostly thought to be small-scale mantle convection driven by several phenomena (e.g., King & Anderson, 1995, 1998; King & Ritsema, 2000; King, 2007; Adams et al.,

252 2018; Ojo et al., 2018). Mount Cameroon is considered the only active volcano with the most recent
253 eruption in 2000 (Tokam et al., 2010).

254   The Central African Shear Zone (CASZ) within the Oubanguides mobile belt formed during the
255 amalgamation of Gondwana and represents the ENE-WSW Precambrian lineament stretching from the
256 Darfur region of Sudan into central Cameroon and disappearing beneath the Oligocene and younger
257 volcanic materials at the southwest end of the CVL. The CASZ is thought to be an extension of the
258 Pernambuco fault in Brazil (Dorbath et al., 1986). To the south of the CVL is the Benue Trough, a failed
259 triple rift junction in Nigeria. Rifting in the Benue Trough started about 140 Ma and continued during the
260 opening of the equatorial Atlantic (119-105 Ma) up until 84 Ma when it underwent a brief period of
261 compression (Fairhead, 1988; Maluski et al., 1995). The Benue Trough was formed in the Proterozoic
262 mobile belts surrounding the Archean Congo Craton and characterized by volcanism between 74-49 Ma
263 (Maluski et al., 1995).

264

265 **3 Data and Methodology**

266 **3.1 Ambient Seismic Noise and Earthquake Data**

267 For this study, continuous ambient seismic noise and earthquake data recorded by 1529 broadband seismic
268 stations belonging to 73 permanent and temporary seismic networks deployed in Africa, Europe, and Arabia
269 over the past three decades are downloaded from the Incorporated Research Institutions for Seismology
270 Data Management Center (IRIS-DMC). Figure 2 shows the distributions of stations and earthquakes. We
271 retrieve daily ambient seismic noise records on the vertical component with a sampling frequency of 1 Hz
272 for the entire lifespan of a station or up until mid-2018. We also retrieve data from earthquakes of $M_W \geq$
273 5.0 with epicentral distances of 30°-120° and depths shallower than 100 km from 1978 to 2018.

274

275 **3.2 Rayleigh Waves from Ambient Noise Cross Correlations and Earthquakes**

276 The data processing procedures to extract fundamental mode Rayleigh waves from ambient seismic noise
277 and earthquake records are well known and fully described in our earlier papers (Ojo et al., 2017, 2018).
278 Here, we provide a brief description of the parameters we employed in this study. We begin with removing
279 the mean, linear trend, and instrument response from the daily ambient noise records, then apply a
280 Butterworth band-pass filter in periods of 5–50 s before partitioning the data into one-hour segments for
281 computational efficiency (e.g., Li et al., 2009). Similar to Bensen et al. (2007), we performed time-domain
282 normalization using the running-absolute-mean method to reduce the influence of earthquakes as well as
283 persistent monochromatic noises (e.g., Xia et al., 2013, 2020; Zeng and Ni, 2011), and a frequency domain
284 whitening over the frequency band of 0.025–0.2 Hz to broaden the frequency spectrum of the ambient noise
285 data and balance the energy. The resulting one-hour-long traces are cross-correlated between all the station

pairs with overlapping operation times and then stacked with their time-reversed cross-correlograms to obtain the symmetrical noise correlation function (NCF). This enhances the Rayleigh-wave signal by suppressing errors due to uneven distributions of the noise field. Finally, we stack all the available cross-correlations for a given station pair to produce the final NCFs used for subsequent dispersion analysis.
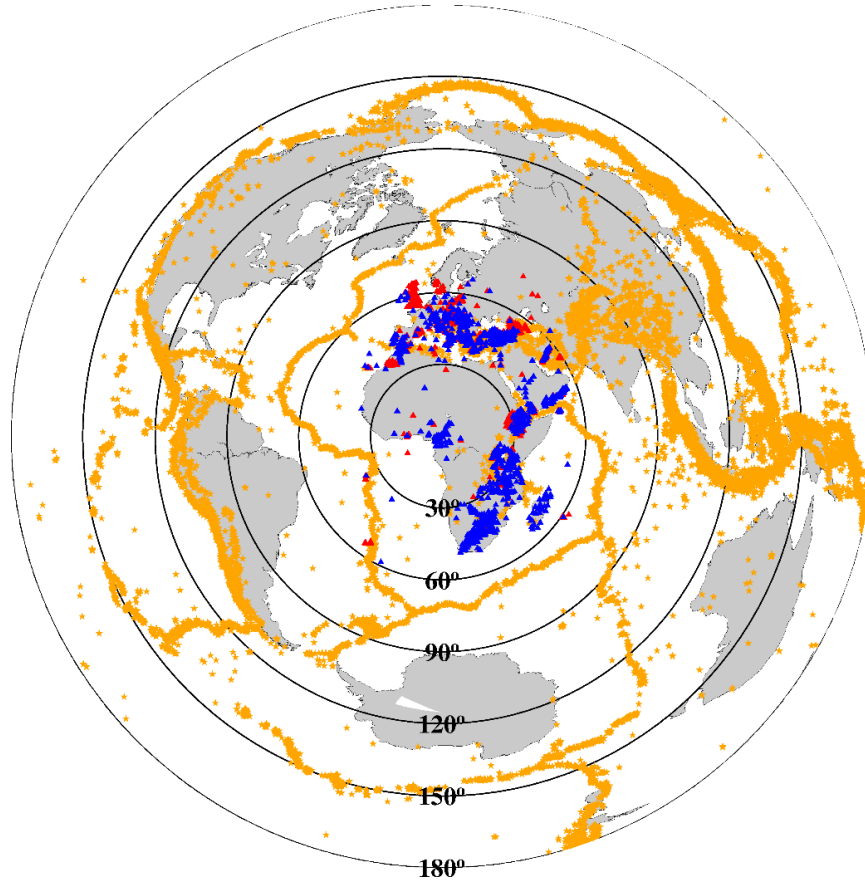

Figure 2. Distributions of broadband seismic stations (blue and red triangles) and earthquakes (yellow stars) used in this study. Red triangles highlight the seismic stations used only in ambient noise analysis. Note the global coverage and good azimuthal distribution of the events used.

To retrieve Rayleigh wave signals from earthquake records, we follow the traditional two-station method (e.g., Chen et. al., 2014; Kästle et al., 2016). As a first step, we select the appropriate event-station pairs that are assumed to travel along the same great-circle path. To achieve this, we set the thresholds in the angle differences between the great circles from the epicenter to the two stations (α) and between the great circles from the epicenter to the nearer station and from the nearer to the farther station (β) to 3° and 7°, respectively (e.g., Yao et al., 2010; Chen et al., 2014; Ojo et al., 2018). Next, we compute the signal-to-noise ratio (SNR) of each seismogram defined as the ratio of the peak amplitude in the signal window to

303 the root mean square of the noise in the noise window, both filtered with a specific central period (Bensen
304 et al., 2007). Waveforms with SNRs less than 5 are discarded. The retained seismograms from the same
305 event recorded by a selected station pairs are narrow-band-pass filtered after removing the instrument
306 responses and cross-correlated to obtain the cross-correlation function (CCF, e.g., Yao et al., 2006). Finally,
307 the positive lag-time sides of the CCFs between the same station pair obtained from all events are
308 normalized and stacked together to obtain the final CCF for each station pair, which in turn, is used as input
309 in the subsequent dispersion analysis.
310

3.3 Dispersion Analysis

312 Using the stacked NCFs and CCFs, we measure the fundamental mode phase and group velocities in the
313 period range of 5–50 s by the automatic frequency-time analysis (AFTAN) with the appropriate phase shift
314 for each dataset (Aki & Richards, 2002; Bensen et al., 2007; Shen & Ritzwoller, 2016). During the
315 dispersion measurement, we use Rayleigh wave phase velocities from the global tomography model of Ma
316 et al. (2014) as a reference to unwrap the 2-pi ambiguity of the phase velocities. We perform quality control
317 to select the reliable dispersion measurements for the subsequent tomography based on the following
318 criteria: (1) The inter-station distance must be greater than one wavelength to ensure sufficient separation
319 of the surface wave packet from precursory arrivals and satisfy the far-field approximation (e.g., Luo et al.,
320 2015). (2) The SNRs of the surface waves must be ≥ 8 to ensure the reliability of the signals. (3) The
321 velocity dispersion data retained at every period must lay within the two standard deviations bound of the
322 mean velocity calculated for all measurements at that period. The last step is to filter out the outliers of the
323 dispersion measurements. Additionally, we visually inspect the dispersion curves to further discard bad
324 measurements that could introduce artifacts in the tomographic inversion. We investigate the discrepancies
325 between the resulting dispersion measurements from the two sources (ambient noise vs. earthquakes) for
326 the same station pair at overlapping periods to understand the possible biases in our dataset. At overlapping
327 periods, dispersion measurements with higher SNR are selected based on the assumption that they are
328 obtained from a better-defined surface wave signal.
329

3.4 Inversion for Phase and Group Velocity Maps

331 To obtain the lateral variation of group and phase velocities in the study area, we perform tomographic
332 inversions for the two-dimensional (2D) phase and group velocity maps at selected periods using the fast-
333 marching surface-wave tomography (FMST) method (Sethian, 1996; Sethian & Popovici, 1999; Rawlinson
334 & Sambridge, 2004, 2005; Rawlinson et al., 2006, 2008). FMST is an iterative nonlinear tomographic
335 inversion method that solves the eikonal equation using the fast-marching method (FMM) based on the
336 finite-difference approximations in a pre-defined grid for the forward modeling in 2D spherical surface

coordinates. A linearized subspace technique is used to solve the inverse problem (Kennett et al., 1988; Rawlinson & Sambridge, 2005). The key benefits of using this method are two-folded: (1) it does not need to repeat the travel-time computation for every ray path as in the traditional ray-tracing methods, and (2) it accounts for the non-linearity of the forward problem to provide stable and robust results even in strongly heterogeneous media (Rawlinson et al., 2010; Fang et al., 2016). We use the average velocity at each period as the starting velocity of the initial model. Since we do not have measurements associated with every station pair, the inverse problem is largely underdetermined, and regularization is needed to provide additional constraints on the model parameters and stabilize the inversion. Our choice of regularization parameters determined by the L-curve method (Aster et al., 2018) routinely favors models with smooth and small lateral velocity variations over models with sharp and large variations at each period.

3.5 Joint Inversion for Shear-wave Velocity Model

From the period-dependent Rayleigh wave phase and group velocity maps, we construct local dispersion curves extracted at 1° x 1° grid spacing and apply a joint inversion program based on the neighborhood algorithm (NA) of Sambridge (1999a,b) as in Ojo et al. (2019). An important advantage of choosing this method over the linearized method (e.g., Herrmann & Ammon, 2004) employed in most previous studies in Africa is its independence from the starting model and its ability to avoid local minimums. The method generates a random initial model based on the user-supplied ranges of model parameters, including layer thickness, velocity, Vp/Vs ratio, density, Qp, and Qs, determined from prior knowledge. The ranges of model parameters used in this study are chosen from literature (Kanamori & Anderson, 1977; Kennett et al., 1995; Brocher, 2005) and are listed in Table 1.

Table 1: Ranges of model parameters used in the NA inversion in this study

Layer ID	Thickness (km)	Top Vs (km/s)	Bottom Vs (km/s)	Vp/Vs	Qp	Qs
Crustal Layer-1	0–2	1.50 –4.00	1.50–4.00	2.00–3.00	100	25
Crustal Layer-2	0–3	1.50–4.00	1.50–4.00	1.65–2.00	675	300
Crustal Layer-3	1–15	2.60–4.50	2.60–4.50	1.65–1.80	1450	600
Crustal Layer-4	5–20	3.20–4.50	3.20–4.50	1.65–1.80	1450	600
Crustal Layer-5	5–20	3.20–4.50	3.20–4.50	1.65–1.80	1450	600
Mantle Layer-1	5 –30	4.00–5.00	4.00–5.00	1.70–1.90	1450	600

The efficient normal-mode formalism of Herrmann (2013) is used to compute the theoretical dispersions in the forward scheme and the objective function is defined as the least-square misfit between the observed and computed dispersions as follows:

$$M_{joint} = \sum_{j=1}^{2} w_j \cdot \sum_{i=1}^{N_j} \left[D_{ij}^{obs} - G_{ij}(m) \right]^2 \tag{1}$$

363

where $j = 1, 2$ refers to the group and phase velocities, respectively, weighted by w_j (with $w_1 = w_2 = 0.5$), $G_{ij}(m)$ and D_{ij}^{obs} are the synthetic and measured velocities, respectively, and N_j is the total number of measurements of a given velocity type. Based on our previous experience, we set the two tunable NA parameters that control how explorative and exploitative the inversion proceeds to be 100 and 60, respectively, and set a maximum of 1000 iterations producing an ensemble of 10100 models for each inversion point. The final 1D Vs model is the mean of all accepted ensemble of models from the surface to 60-km depth at each grid and the standard deviation is used to quantify the model uncertainty. At each grid point, we obtain an estimate of the crustal thickness by summing the thicknesses of the inverted crustal layers in the model ensemble and computing its mean and standard deviation.

4 Results and Interpretation

4.1 Emergence of Rayleigh Waves from Ambient Noise Cross Correlations

Figure 3 shows an example of the cross-correlations between the vertical-component ambient noise and earthquake records at station G.ATD and 46 other selected stations. Both the NCFs and CCFs yield a clear wave packet with a linear trend in arrival times, representing the fundamental mode Rayleigh waves with a moveout velocity of ~3.4 km/s (Shapiro & Campillo, 2004). Despite the different energy sources and methodology, the similarity in the symmetric NCFs and CCFs and dispersion curves indicates that both methods yield the same result and justifies the joint employment of the two datasets. Therefore, we combine them in the subsequent inversions to improve the resolution and achieve sensitivity to a broader depth range than previous studies (e.g., Kästle et al., 2018; Pourpoint et al., 2018).
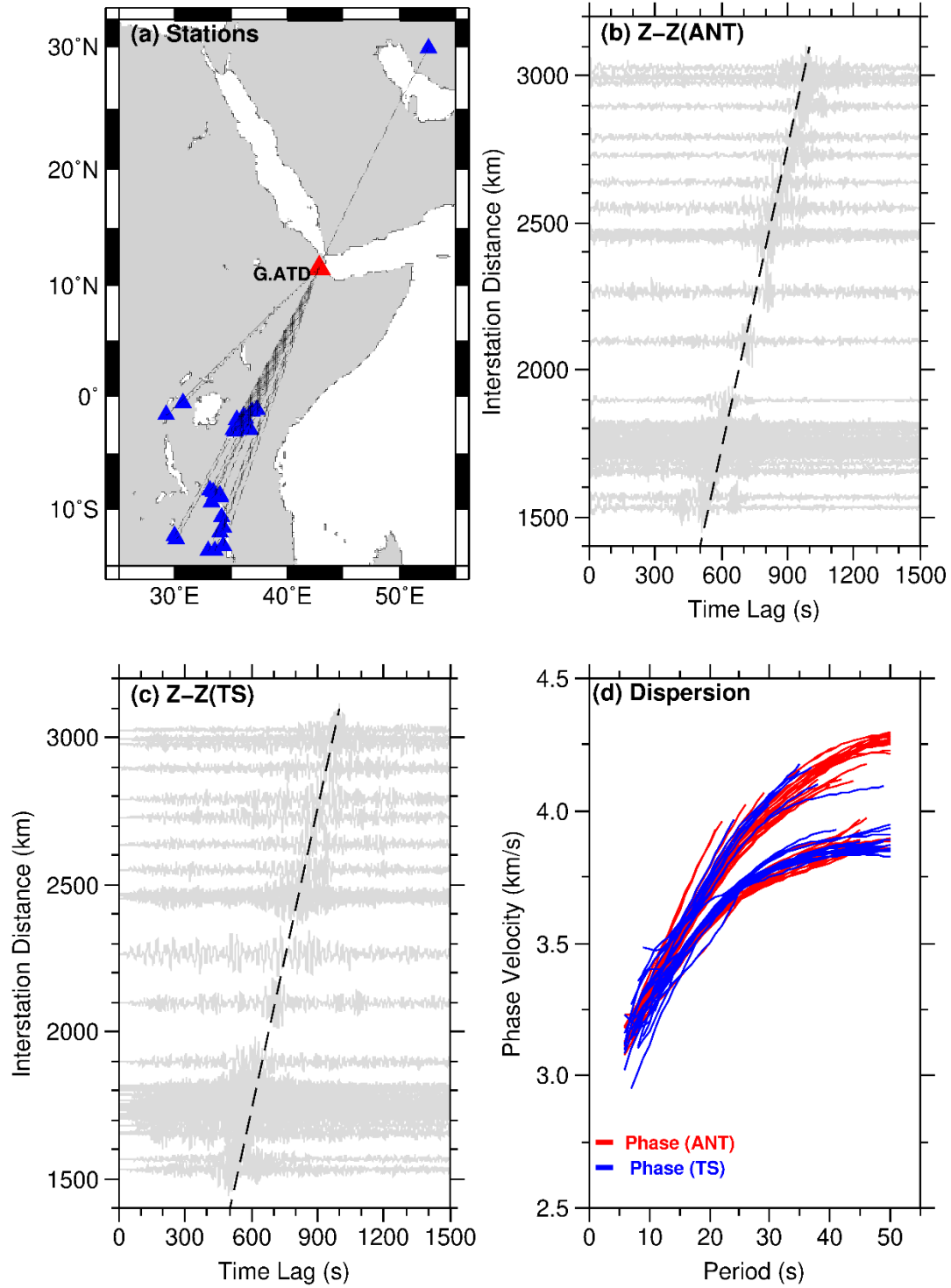
Figure 3. (a) Ray paths (thin black lines) between station G.ATD (red triangle) and 46 other seismic stations (blue triangles) and representative stacked (b) NCFs and (c) CCFs filtered between 10 and 30 s (d) Phase dispersion data retrieved from the NCFs and CCFs waveforms. The black dashed line indicates the arrival times of the Rayleigh waves with a moveout of ~3.4 km/s.

14

4.2 Ray Path Coverage Improvement and Dispersion Discrepancy

Figure 4(a) shows the total number of paths available at each period in the final dataset used for the tomographic inversion after removing traces that do not meet the selection criteria mentioned in Section 3.3. The phase and group velocity measurements from the NCFs reveal two characteristic peaks corresponding to the primary (10–30 s) and secondary (5–10 s) microseisms. As expected, the maximum number of paths obtained is highest at short periods (< 15 s) for NCF measurements and at longer periods for the CCF analysis. To improve the resolution of the subsequent tomographic inversion, we combine the phase and group velocity measurements from NCFs and CCFs and achieve a significant improvement in the path coverage at overlapping periods (red in Figure 4a). The peak number of paths increases from ~25,000 (~15 s from NCFs) and ~30,000 (~25 s from CCFs) to ~50,000 at ~20 s when combined, enabling us to image the African continent at an unprecedented resolution. Figures 4(b-d) show the differences between the phase and group velocities obtained from NCFs and CCFs at overlapping periods of 15 s, 20 s, and 30 s. For dispersion measurements with high SNRs $\geq$ 10, the distribution of the phase-velocity differences follows a Gaussian distribution centered around ±0.01 km/s at 20 s and 30 s period and -0.02 km/s at 15 s; the mean differences are slightly larger for group velocity (-0.08 km/s at 15 s and 20 s, and -0.11 km/s at 30 s). The relatively small standard deviations suggest that the two types of measurements are consistent with each other and well within the typical range of uncertainties in dispersion measurement, i.e. ~1.5-1.7% of the average velocity (e.g., Yao et al., 2006, 2010; Ojo et al., 2018). The observed discrepancy can be attributed to different data sensitivity to heterogeneities and methodology (de Vos et al., 2013).
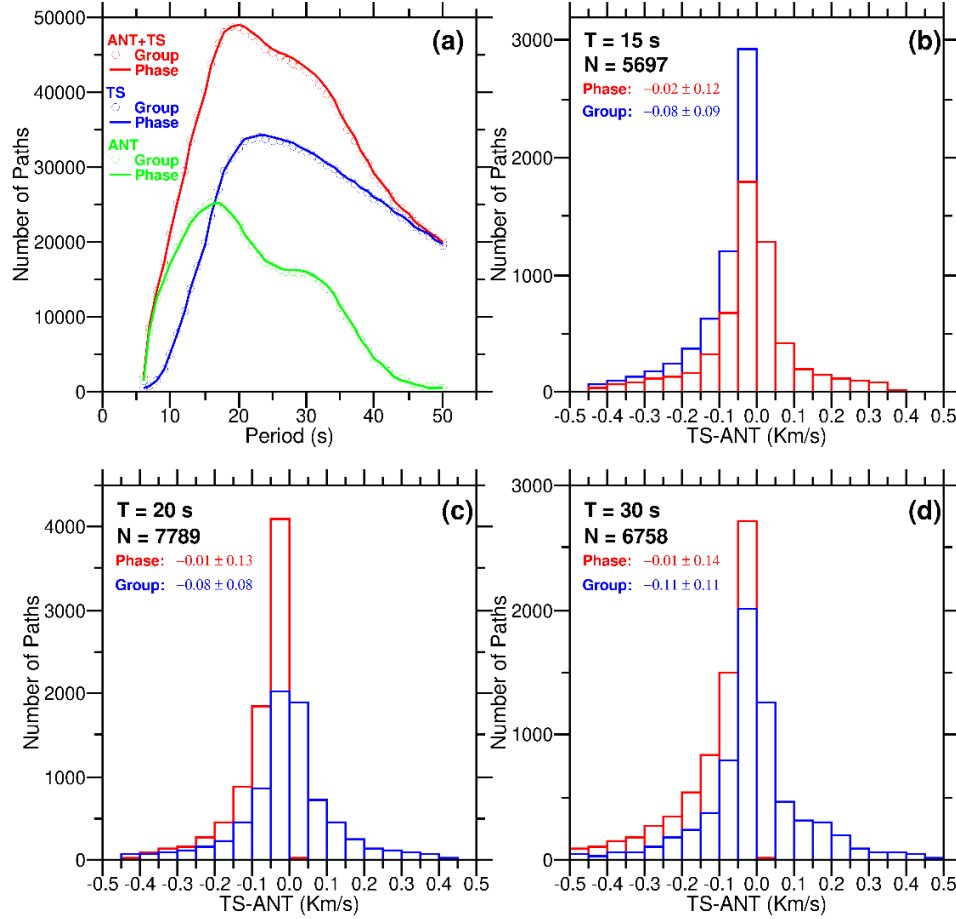
409

410 **Figure 4**. (a) Ray path count vs. period for the phase (solid lines) and group (circles) velocity measurements

411 obtained from records of ambient seismic noise (NCFs, green) and earthquakes (CCFs, blue). The total

412 number of paths of the combined NCF and CCF datasets is shown in red. (b), (c) and (d) Histograms of ray

413 path count for phase (red) and group (blue) velocity measurements at overlapping periods of 15 s, 20 s, and

414 30 s, respectively. The total number of paths (N) at each period is given for comparison. The mean

415 differences (km/s) between the NCF and CCF measurements and standard errors (km/s) are also noted for

416 phase and group velocities.

417

418 **4.3 Checkerboard Tests**

419 Despite its potential drawbacks, the checkerboard test is still valuable for investigating the capability of a

420 given station configuration to resolve the velocity structure across the study region (e.g., Leveque et al.,

421 1993; Simons et al., 2002; Rawlinson & Spakman, 2016). Therefore, we perform checkerboard tests at

422 different periods for varying cell sizes using the same inter-station ray paths for the observed data and the

423 optimal regularization parameters (e.g., Humphreys & Clayton, 1988; Inoue et al., 1990; Zhao, 2015). By

424 varying the cell size from 0.5° x 0.5° to 5° x 5° at an interval of 0.5° and reconstructing the checkerboard

425 based on the ray paths in the real dataset at different periods, we find the cell size of 3° x 3° to be the

426   minimum grid size that allows for satisfactory recovery of the checkerboard model across the entire
427   continent. The checkerboard is not well resolved at smaller cell sizes especially at regions with sparse
428   seismic stations (Figure 2). Figure 5(a) shows the 3° x 3° input model with a checkerboard pattern defined
429   by peak velocity perturbations of ±0.4 km/s relative to the average velocity at each period and a bi-cubic
430   B-spline interpolation between grid-nodes. Representative examples of the recovered checkerboard models
431   with 3° x 3° cell size for group and phase velocities at periods of 8 s, 20 s, 30 s, and 50 s are provided in
432   Figures 5(b-i). A comparison of the recovered checkerboard results to the input model gives us a basic
433   impression of the different resolving powers by the data at different periods across the continent. At shorter
434   periods (≤ 8 s; Figures 5b&c), the numbers of selected ray paths are insufficient to accurately resolve the
435   3° x 3° checkerboard pattern in the main part of northern Africa which is sparsely instrumented (see Figure
436   2). Signs of smearing with elongated anomalies trending in the NW-SE direction are obvious in the
437   reconstructed models, indicating a deterioration in the resolution power. The ray path density becomes
438   progressively improved with increasing periods, achieving the best ray path coverage at periods between
439   20 s and 30 s, and dropping again towards the longest period used in the study (see Figures 5d-i). As
440   expected, we are unable to recover the checkerboard in areas outside of the data coverage. Because the
441   lateral resolution is closely linked to the density and distribution of local stations as well as the number of
442   ray paths, the checkerboard patterns are better resolved at all periods and cell sizes in eastern and southern
443   Africa and southern parts of Europe. Meanwhile, the checkerboard test also demonstrates that the goal of
444   this study to image the lithospheric structure in sparsely instrumented regions of the African continent is
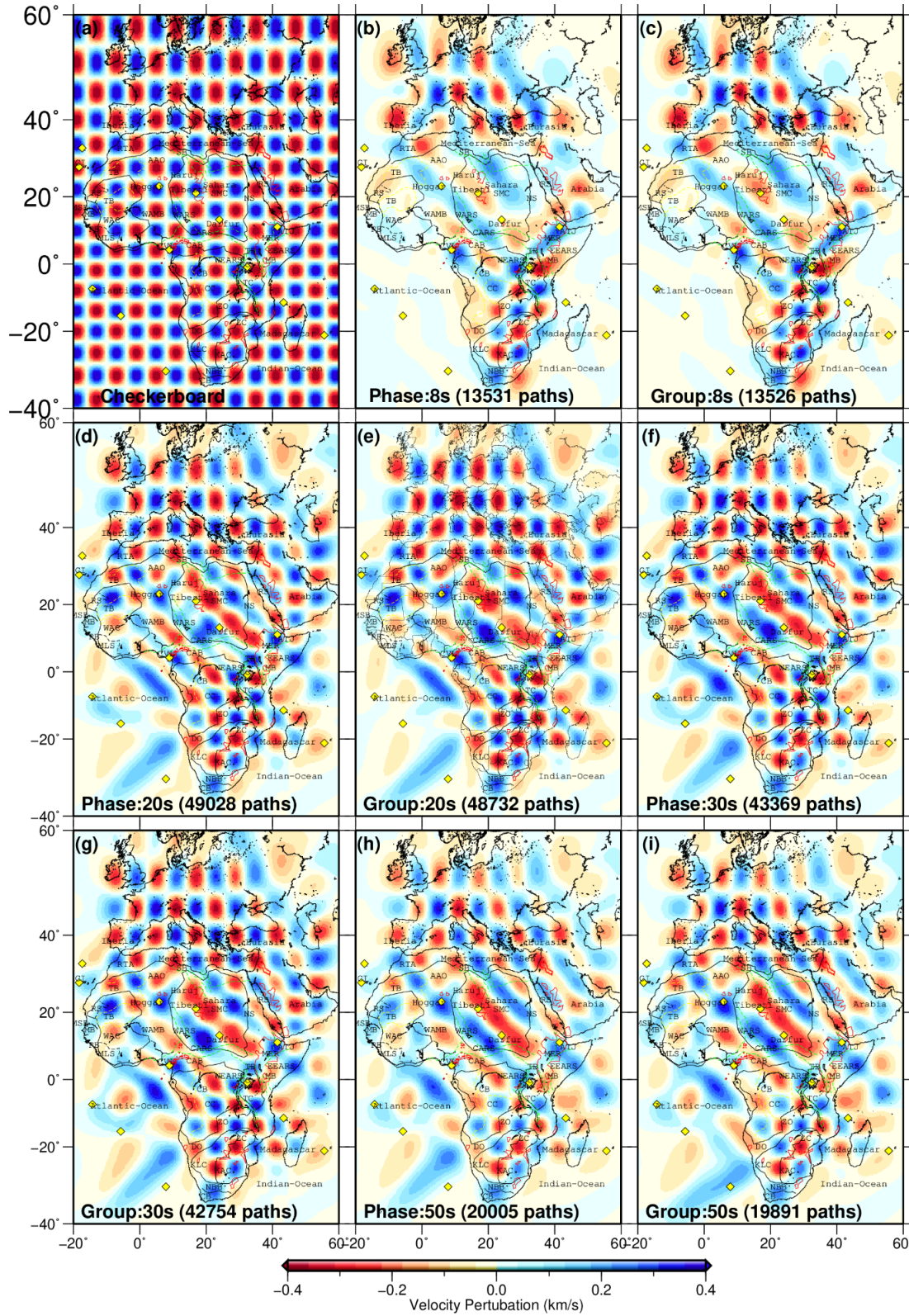445   achievable with the available dataset.

446

Figure 5. Checkerboard resolution test. (a) Checkerboard input model with a cell size of 3° x 3° and peak velocity perturbation of ±4%. (b-i) Recovered models of Rayleigh wave phase and group velocities at

449 periods of 8 s, 20 s, 30 s, and 50 s. Overlain on the plots are the geometry and locations of the main

450 geological features across the study area as defined in Figure 1.

451

452 **4.4 Phase and Group Velocity Maps**

453 Figure 6 presents the Rayleigh wave phase and group velocity maps, and depth sensitivity kernels for

454 periods of 10 s, 20 s, and 40 s. The depth sensitivity kernels indicate the depth ranges that contribute to the

455 frequency-dependent velocity maps. Here, we simply provide a general description of the main features in

456 the apparent velocity models, and interpretations of the inverted three-dimensional (3D) Vs models in terms

457 of regional tectonics are presented in the subsequent sections.

458 At shorter periods (e.g., 10 s; Figures 6a&b), the peak sensitivities are in the range of ~0–10 km depth,

459 and the phase and group velocity anomalies are generally consistent with surface geology with high

460 velocities coinciding with cratonic units (e.g., KAC, ZC, TC, and UC) and low velocities in basins (e.g.,

461 CB, TB, and SB) underlain by thick sediments, as well as passive margins and hotspots (Figures 6a&b)

462 (e.g., Yang et al., 2008; Domingues et al., 2016; Accardo et al., 2017; Pratt et al., 2017; Adams et al., 2018;

463 Fadel et al., 2018; Adimah & Padhy, 2019; Chambers et al., 2019; Wang et al., 2019; Thybo et al., 2019).

464 Outside of the African continent, the Arabian plate shows two distinct anomalies, fast velocity within the

465 shield and low velocity farther into the interior platform (e.g., Tang et al., 2016; Yao et al., 2017; Kaviani

466 et al., 2020). In southern Europe, the eastern Mediterranean Sea reveals a much lower velocity than the

467 western part, and the Apennines are clearly outlined by low velocity (e.g., Yang et al., 2007; Kästle et al.,

468 2018; Lu et al., 2018; Manu-Marfo et al., 2019).

469 At intermediate periods (e.g., 20 s; Figures 6c&d), the depth sensitivities peak in the ~10–25 km depth

470 range and the resolution are more uniform due to increased ray paths (see Figure S1). The velocity maps

471 show a general increase in velocity with depth, with fast anomalies in regions of relatively shallow oceanic

472 crust (e.g., western Mediterranean and the Red Sea), rift zones (e.g., WARS), and cratonic units; while slow

473 anomalies still coincide with regions of thick sediments, mobile belts and hotspots (e.g., Darfur).

474 At longer periods (e.g., 40 s; Figures 6e&f) corresponding to a greater depth, the velocity maps are

475 more consistent with uppermost mantle structure and variations in the crustal thickness. Fast anomalies

476 generally coincide with regions underlain by relatively thin crust while slow anomalies correspond to

477 regions of relatively thick crust. Based on the normalized ray path densities, the resolution of the maps is

478 poorest in the northwestern part of Africa and the surrounding oceans and best in eastern and southern

479 Africa and southern Europe (see Figure S1). Generally, the pattern of anomalies on the group and phase

480 velocity maps are similar at each period with slight differences that may be related to different depth
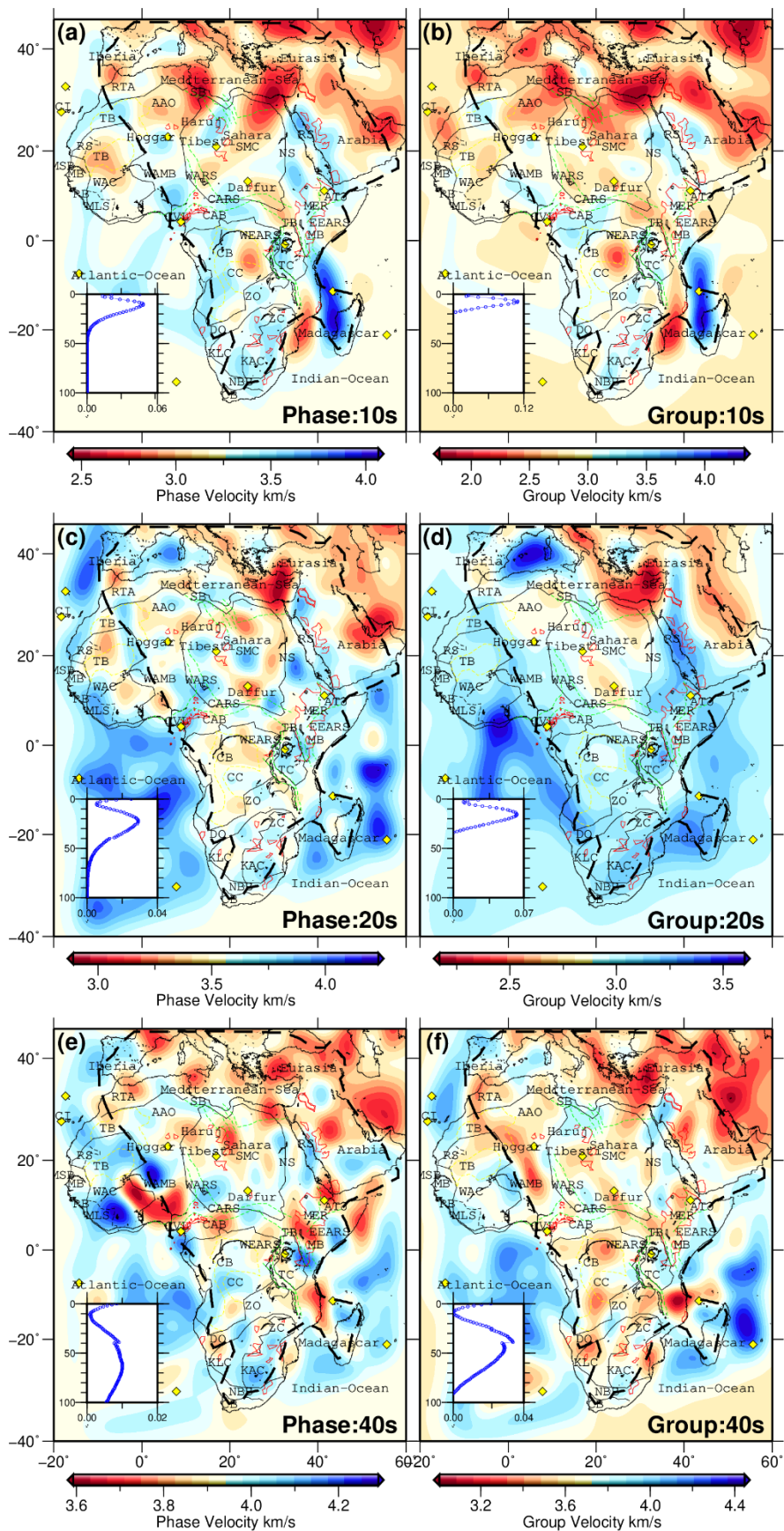
481 sensitivities.

Figure 6. Maps of phase (a, c, e) and group (b, d, f) velocities at periods of 10 s, 20 s, and 40 s, with the inset plots showing the depth sensitivity kernels at the respective periods. Overlain on the plots are the geometry and locations of the main geological features across the study area as defined in Figure 1. The thick black dash line denotes the areas of the maps that are best resolved based on the ray path density.

4.5 1D Vs Models from Joint Inversions

In Figure 7, we present examples of the joint inversion result at four grid points located in different tectonic settings in western, eastern, northern, and southern Africa. Figure 7(a) shows the inverted Vs model along the CVL in western Africa characterized by low Vs at shallow depths underlain by a gradual increase of Vs with depth and the Moho at the depth of ~35 km. Figure 7(b) depicts a typical 1D Vs model within the cratonic units in southern Africa. The crust is relatively thick (~37 km) and characteristically fast Vs (~4 km/s) typical of cratonic crust can be seen from the upper crust down to the uppermost mantle. The Vs model in Figure 7(c) in eastern Africa near the Afar triple junction is characterized by a slow Vs (< 2.5 km/s) at shallow depths that persists down to the middle crust, typical of regions with active volcanism where magma exists within the crust (e.g., Chambers et al., 2019). Figure 7(d) shows an example of the inverted Vs model within the Rif-Tell-Atlas mountain belts in northern Africa, which reveals a relatively slow Vs at shallow depths underlain by a gradual increase of velocity with depth. The crustal thickness is ~39 km. Generally, we obtain characteristically smooth models that are geologically more plausible and consistent with the tectonic settings.
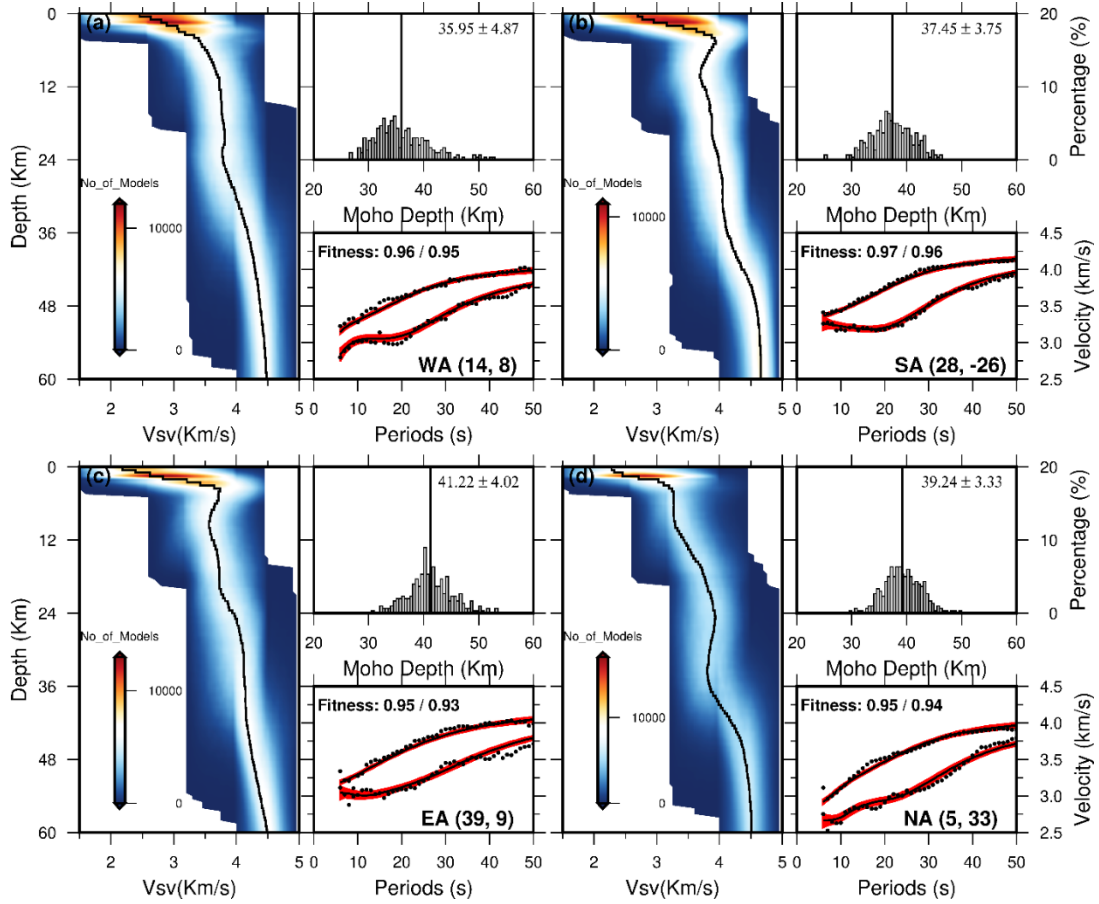
Figure 7. 1D Vs model jointly inverted from group and phase velocity data at four representative grid points located in (a) the CVL in western Africa, (b) the Kaapvaal craton in southern Africa, (c) the Afar Triple Junction in eastern Africa, and (d) the Rif-Tell-Atlas mountain belts in northern Africa. For each location, the left panel shows the mean 1D Vs model in a thick black line against the background of the ensembles of the 1D models sampled by the neighborhood algorithm. The upper-right panel displays the range of crustal thickness estimated from the 300 best-fitting models and the mean value (vertical black line) with associated uncertainty. The lower-right panel shows the observed dispersion data in black dots and predictions by the 300 best-fitting models and the mean Vs model in red and black lines, respectively. Also noted on the plot are the misfit values between the observed data and their theoretical predictions by the mean model.

4.6 Model Misfit

In Figure 8 we present the misfits between the group and phase velocity measurements and their theoretical counterparts predicted by the mean 1D Vs models at all grid points, following Ojo et al. (2019). A value of zero means a perfect fit between the theoretical and observed velocities while increasing values up to unity indicate a worsening fit. Figure 8 shows that at most grid points the misfit values are less than 0.1, and

22

519 much lower values are seen in regions with dense seismic stations. The group velocity seems to have a
520 slightly larger misfit than the phase velocity, indicating a better fit by the final Vs model to the phase
521 velocity measurements. A maximum misfit of 0.25 across the study area illustrates the overall goodness of
522 data fit achieved in this study. It also demonstrates the robustness of the inversion scheme as well as the
523 model parameterization which allows for satisfactory fits to both datasets for most of the study region (Ojo
524 et al., 2019). The slightly larger misfit values beneath the sedimentary basins and surrounding oceanic
525 regions indicate that it is necessary to investigate more closely the appropriate ranges of model parameters
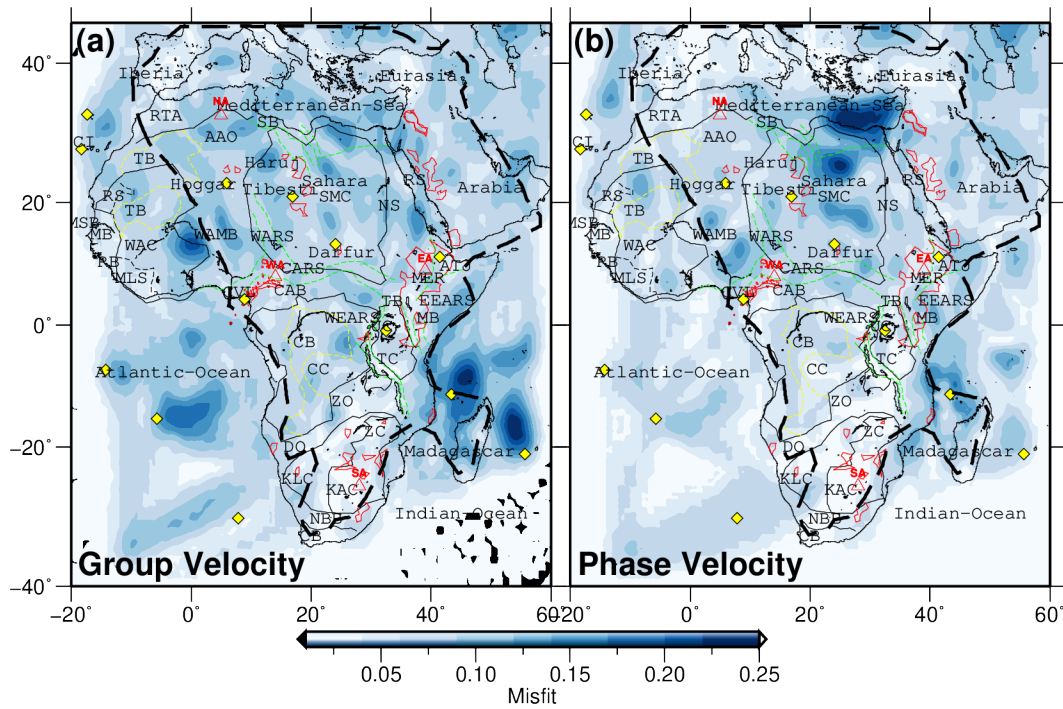526 (Table 1) needed to fit the dataset at those locations.

527

528 **Figure 8**. Maps of the misfits in (a) group and (b) phase velocities between the predictions by the mean 1D
529 Vs model and the observed data. Red labels and triangles represent locations where joint inversion examples
530 are presented in Figure 7. Overlain on the plots are the geometry and locations of the main geological
531 features across the study area as defined in Figure 1. The thick black dash line denotes the areas of the maps
532 that are best resolved based on the ray path density.

533

534 **4.7 General Features of the 3D Vs Model**

535 In Figure 9, we present the 3D Vs model at different depth ranges from the surface to the uppermost mantle.
536 We divided the estimated crustal thickness (CT) into three equal thicknesses at each grid point and the
537 average velocity at these depth ranges as proxies for the upper (0 - 1/3CT), middle (1/3CT – 2/3CT), and
538 lower (2/3CT – CT) crust. Likewise, we define the uppermost mantle by averaging the velocity from the

23

539 estimated crustal thickness to the bottom of the model (CT – 60 km). We focus on structures within the

540 defined region of best resolution denoted by the black thick line in Figure 9 to avoid interpreting possible

541 artifacts.

542   In the upper crust (Figure 9a), relatively slow Vs (≤ 3 km/s) anomalies are observed at locations

543 underlain by thick sediments (e.g., TB, CB, SB, Tyrrhenian Basin, Arabian Platform, etc.) and along zones

544 of active deformation (e.g., MER, WARS, CARS, AAO, SMC, etc.) while relatively fast Vs (≥ 3.5 km/s)

545 anomalies mainly coincide with cratons (e.g., KAC, ZC, UC, TC, etc.; Ebinger et al., 2017). The estimated

546 sediment thickness in the uppermost crust ranges from 0 to 14.5 km and is consistent with the estimates of

547 Laske & Masters (1997) across the study area (details in Text S1 and Figure S2). The structure in the mid

548 crust (Figure 9b) shows a general increase in Vs in comparison to the upper crust but tends to be less

549 heterogeneous (i.e. small velocity perturbation < 1 km/s). However, relatively fast Vs (≥ 4.0 km/s) can be

550 observed at locations underlain by thin crust (e.g., Red Sea, etc.), along the edges of the Arabian plate,

551 mobile belts, and orogens (e.g., WAMB, AAO, DO), Rift zones (e.g., CARS), and cratons (e.g., KAC).

552 Relatively slow Vs (≤ 3.7 km/s) is pronounced within the Saharan metacraton and associated hotspots,

553 Arabian Platform, eastern Tyrrhenian Basin, and around the Afar Tripple Junction (Figure 9b).

554   In the lower crust (Figure 9c), prominent fast Vs (≥4 km/s) anomalies are observed along the Red Sea,

555 WAMB, western-to-central Mediterranean Sea. We also found thick layers (~5 – 15 km) of high-velocity

556 (Vs ≥ 4.0 km/s) beneath cratonic units (e.g., WAC, CC, KAC), areas characterized by compressional and

557 extensional tectonics (e.g., EARS, CARS), and locations of hotspot centers and diamond-rich

558 kimberlites/lamproites, indicating the presence of mafic, high-density materials (details in Text S2 and

559 Figure S2). Relatively slow Vs (≤ 4.0 km/s) is obvious beneath volcanic centers (e.g., Hoggar, Tibesti, and

560 Darfur), western EARS, MER, southern Madagascar Island, northern CC, AAO, CB, and beneath some

561 cratonic units (e.g., UC and ZC; Figure 9c). At this depth range, the spatial variation in Vs is strongly related

562 to the crustal thickness across the study area, and the slow Vs may be in regions of thicker crust, while fast

563 Vs may exist in regions of thinner crust. The estimated crustal thickness ranges from ~19 to 55 km and

564 varies greatly both among and within the tectonic provinces of the African continent and the surrounding

565 regions (details in Text S3 and Figure S3). In the uppermost mantle (Figure 9d), most of the study area is

566 characterized by Vs ≥ 4.5 km/s. However, localized slow Vs (≤ 4.2 km/s) anomalies are found at several

567 locations (e.g., WAMB, MER, SMC, RS, EARS, DO, SMC, TB, MB, TC, eastern Malawi Rift, and

568 southwestern Madagascar; Figure 9d).

569   A detailed comparison of our 3D model with existing models from global/continental-scale studies

570 (e.g., Laske et al., 2013; Schaeffer & Lebedev, 2013; Moulik & Ekstrom, 2014; Pasyanos et al., 2014; Celli

571 et al., 2020) indicate greater agreement at mid-lower crustal and uppermost mantle depths within the

572 estimated uncertainty of our model (details in Text S5; Figures S4 & S5). However, at upper crustal depth

573 and in sparsely instrumented regions of north-central and southwestern Africa, our model reveals more
574 detailed features that correlate better with known tectonic features and we discussed this further in Section
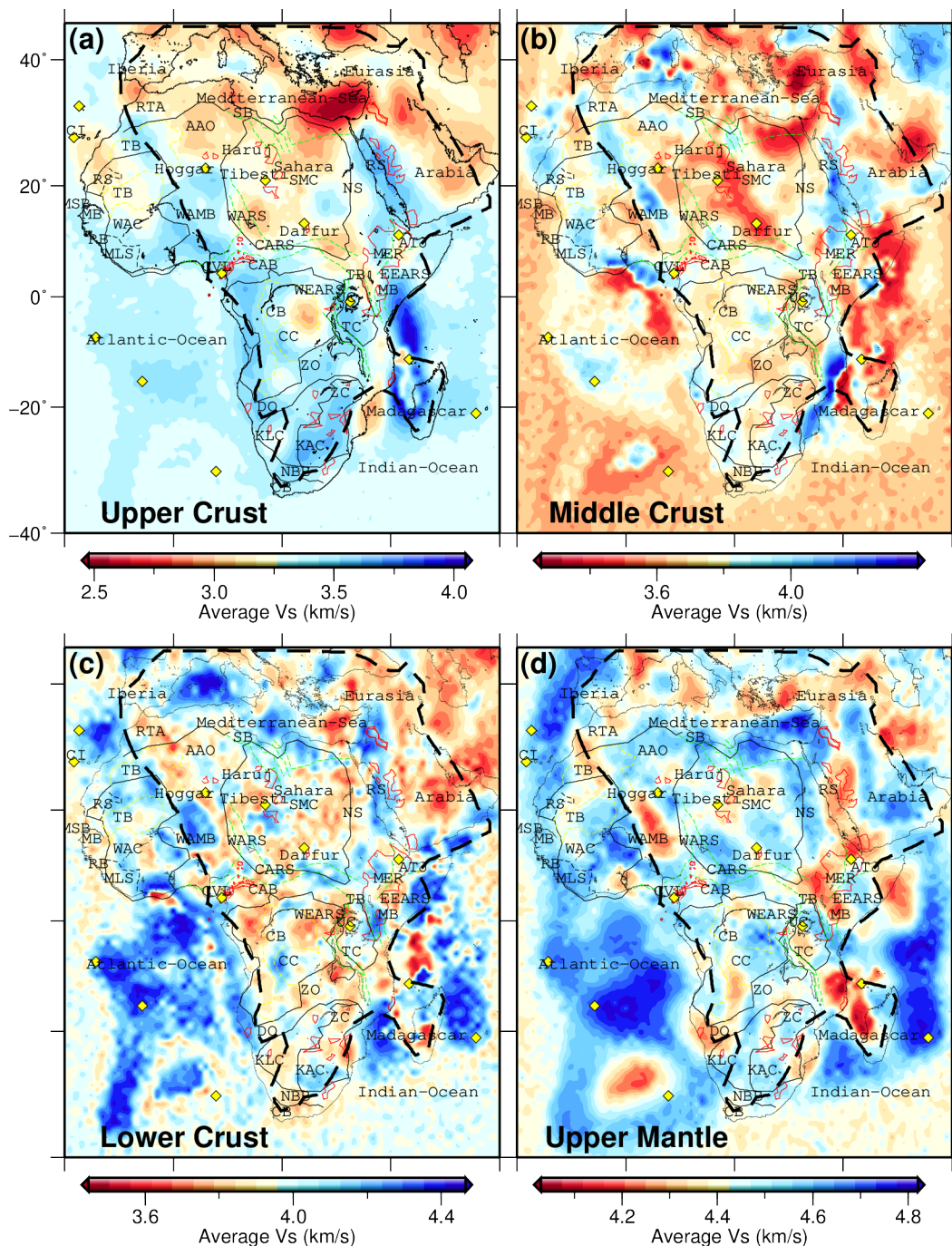575 5.1

576

577 **Figure 9**. Shear wave velocity maps in four depth ranges across the study area. Vs anomalies are averaged
578 over depth ranges within (a) the upper crust (b) the middle crust, (c) the lower crust, and (d) the upper
579 mantle. See text for the definition of the depth ranges. Overlain on the maps are the geometry and locations

580 of the main geological features across the study area as defined in Figure 1. The thick black dash line

581 denotes the areas of the maps that are best resolved based on the ray path density.

582

583 The average uncertainties at crustal and uppermost mantle depths range between 0 to 0.6 km/s but

584 are generally less than 0.2 km/s in most of the study area as shown in Figures 10. The uncertainties reduce

585 with increasing period included in the study reflecting the advantage of including dispersions from

586 earthquake data. The map in the uppermost crust (Figure 10a) is characterized by slightly higher

587 uncertainties (up to 0.3 km/s within the continent) while the map at uppermost mantle depths (Figure 10d)

588 is associated with the lowest uncertainties ($\leq$ 0.2 km/s).

589

590 **4.8 Cross-sections Traversing Major Tectonic Blocks of Africa**

591 For a more detailed description of the features in the 3D Vs model, we present four cross-sections traversing

592 different tectonic regions in Africa and surrounding regions in Figure 11. The north-south profile AA' in

593 Figure 11(a) traverses from the Cape belt, Namaqual-Natal and Kaapvaal craton in southern Africa through

594 the Zambezi Orogen, the Congo craton, Central African belt, the Dafur hotspot, the Saharan metacratons

595 into the Mediterranean Sea, and ends in the Alpinnes in southern Europe. A layer of slow Vs ($\leq$ 3 km/s)

596 delineates the location, geometry, and depth extents of sediments beneath different tectonic regions in the

597 African uppermost crust. Low Vs is obvious down to ~15 km depth beneath the Congo craton, revealing

598 the presence of thick sediment (e.g., Laske & Master, 1997; Figure S2). Similarly, low Vs extends

599 progressively to greater depths from the Saharan desert into the northern margins, reaching to more than 15

600 km beneath the eastern Tyrrhenian Basin which is characterized by thick sediments (e.g., Lu et al., 2018).

601 Underlying the Congo and Tyrrhenian Basin is a relatively shallow crust featuring fast Vs ($\geq$ 4.2 km/s).

602 Also, fast Vs (~4 km/s) is seen at both shallow and greater depths beneath the cratonic region (KC). Shear

603 wave velocity is relatively slower beneath the Darfur region into the mid-lower crust, and a localized fast

604 Vs layer is seen within the Saharan metacraton in this depth range. The lowermost crust reveals fast Vs ($\geq$

605 4 km/s) across the profile with varying thickness. Relatively fast Vs in the upper mantle is seen beneath the

606 craton (KAC) and basins (CB and Tyrrhenian Basin) while the surrounding mobile belt reveals a relatively

607 lower Vs. Shear wave velocities are slow ($\leq$ 4.3 km/s) throughout the uppermost mantle beneath the Darfur

608 hotspot and the Alpine region. The Moho depth varies across the profile with relatively shallow Moho (~30

609 km) beneath the Sahara metacraton and deep one (~45 km) beneath the Congo Basin.
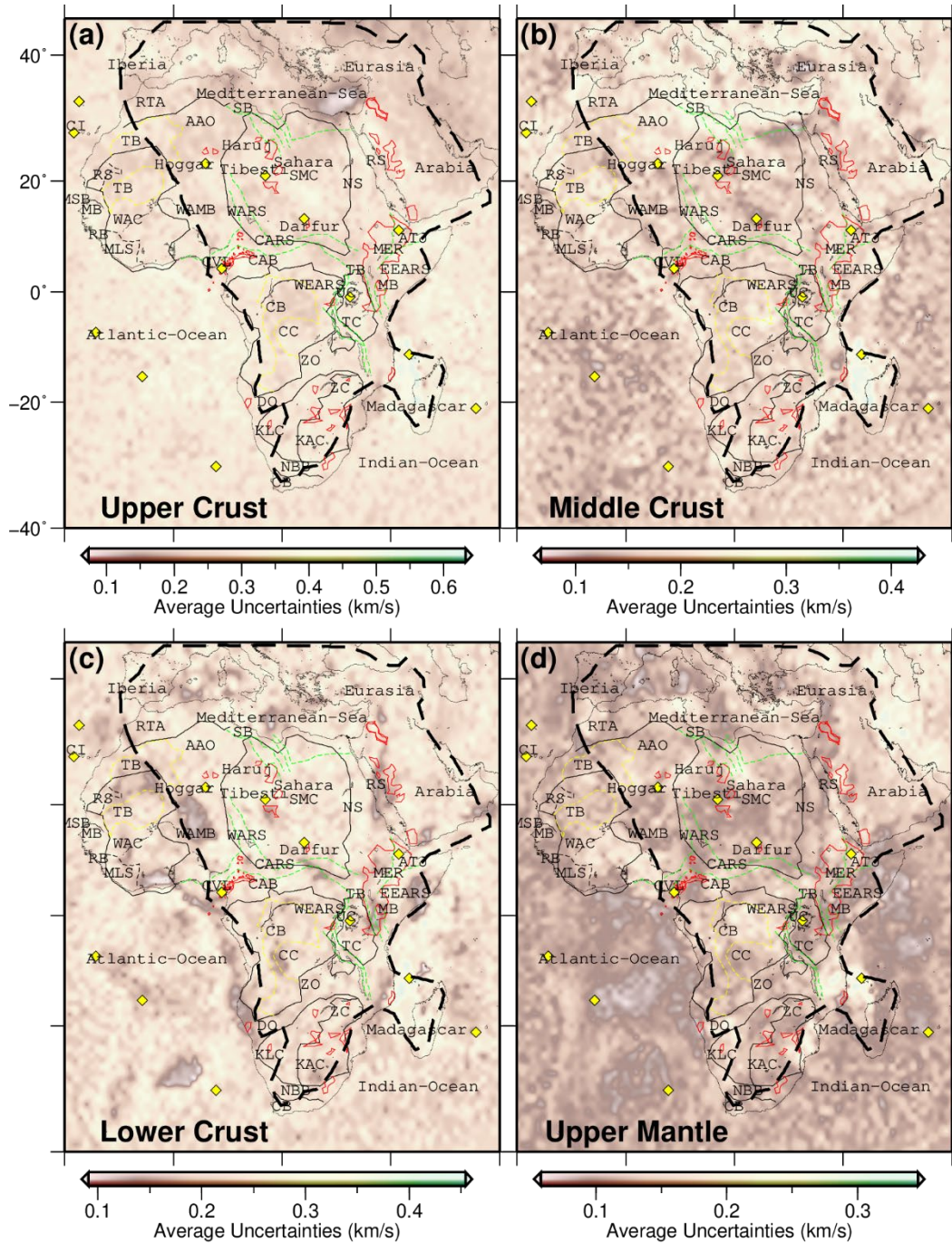
Figure 10. Average uncertainties of the 3D Vs model in four depth ranges across the study area. (a) the upper crust (b) the middle crust, (c) the lower crust, and (d) the upper mantle. See text for the definition of the depth ranges. Overlain on the maps are the geometry and locations of the main geological features across the study area as defined in Figure 1. The thick black dash line denotes the areas of the maps that are best resolved based on the ray path density.
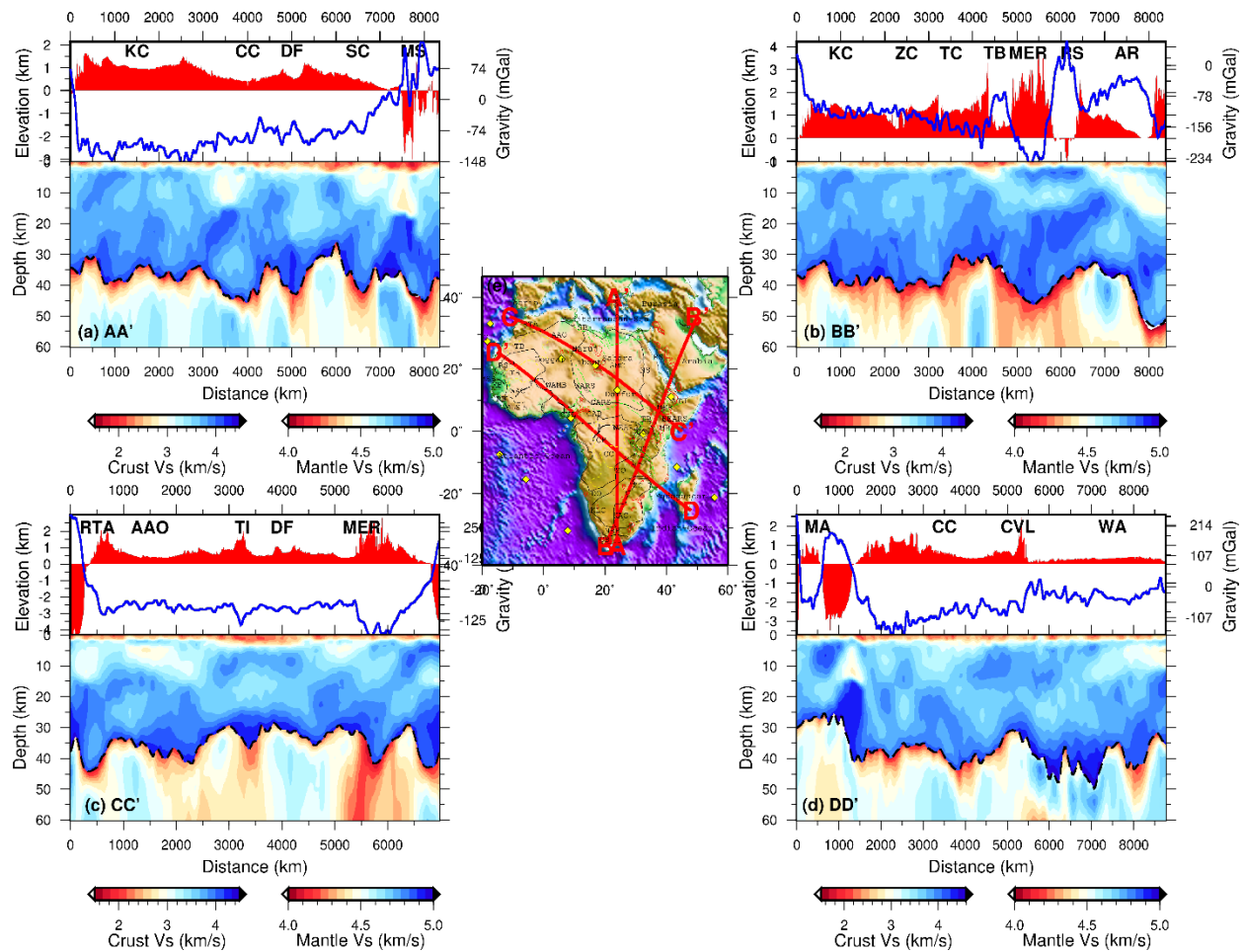
Figure 11. Cross-sections from the surface to 60-km depth along profiles (a) AA', (b) BB', (c) CC', and (d) DD'. (e) Map of study region showing locations of the profiles in (a-d). Plotted on top of each cross-section is the elevation from ETOPO1 (Amante & Eakins, 2009) in red and the Bouguer gravity anomaly (EIGEN-6C4, Förste et al., 2014) profile in blue. The yellow diamonds in (e) mark locations of hotspots in the study region and labels in black denote the main tectonic features as defined in Figure 1.

Profile BB' (Figure 11b) traverses from the Cape belt, Namaqual-Natal, and the cratonic units in southeastern Africa (KAC, ZC, and TC) into the Main Ethiopian Rift, the Afar Triple Junction, the Red Sea, and the Arabian plate. A very thin layer of slow Vs (≤ 3 km/s) is present across most of the profile but extends to greater depths beneath thick sedimentary regions such as the Turkana Basin (~5 km) and the Arabian platform (~ 20 km). Fast Vs (≥ 4km/s) characterizes the entire cratonic region down to the Moho (~40 km), with a relatively shallower depth beneath the Tanzania craton (~35 km). A localized fast Vs layer is obvious beneath the MER and the Red Sea, which may represent mafic bodies that cooled down within the crust during magma eruption (e.g., Ebinger et al., 2017). Relatively slow Vs (≤ 4.4 km/s) is observed in the uppermost mantle beneath the EARS, MER, and the Red Sea with evidence for magmatic underplating

28

634 and accompanying crustal thickening (~45 km/s). A similar observation is made at the edge of the profile

635 beneath the Mesopotamian Foredeep Basin in eastern Arabia (e.g., Kaviani et al., 2020). Fast uppermost

636 mantle Vs (≥ 4.6 km/s) is generally observed at greater depths within the mantle beneath the cratons (KC,

637 TC, and UC) except for the Zimbabwe craton and the Arabian shield. The crust is relatively thin (~35 km)

638 beneath the Arabian shield and thickens towards the Arabian platform and Mesopotamian Foredeep Basin

639 (e.g., Kaviani et al., 2020).

640 Profile CC' in Figure 11(c) begins at the passive margin, enters the Rif-Tell Atlas mountain and the

641 Anti-Atlas Orogen, crosses the West African Mobile Belt into the Saharan metacraton, Central African

642 Belt, Ethiopian Plateau, and MER, then terminates at the eastern EARS. A thin layer of slow Vs (≤ 3 km/s)

643 is obvious in the uppermost crust which persists to a greater depth (~ 5 km) beneath the Saharan metacraton

644 and volcanic centers. A very thin layer of relatively fast Vs exists beneath the passive margin, Anti-Atlas

645 Orogen, WAMB, and CAB but underlain by relatively slow Vs (≤ 3.2 km/s) down to a depth of ~15 km

646 except for CAB where the slow Vs stops at ~8-km depth. We interpret the slow Vs beneath the passive

647 margin as evidence for thick sediment, while the orogen and shear zone as an indication for a weakened

648 crust. Localized fast Vs (≥ 4 km/s) zones are obvious beneath the Saharan Metacraton, probably indicating

649 the presence of cratonic fragments or cooled mafic magma beneath the hotspots in the upper crust (e.g., Ojo

650 et al., 2019). The lower crust along the profile is generally characterized by fast Vs (≥ 4km/s). The Moho

651 is relatively deep beneath the Rif-Tell Atlas mountain (~45 km), consistent with isostatic compensation.

652 The Moho is at ~43-km depth beneath the MER and plateau, and shallower beneath the Saharan

653 metacratons, Darfur region, and eastern EARS (~30–35 km). Pronounced slow upper mantle Vs (≤ 4.4

654 km/s) is seen beneath the MER and eastern EARS, indicating the presence of high temperature and partial

655 melting or upwelling of magma probably from the sub-lithospheric mantle (e.g., Civiero et al., 2016;

656 Chambers et al., 2019). The overlying deep Moho may reflect ongoing magmatic underplating, the

657 continued addition of mafic material to the base of the lower crust. Similarly, relatively slow Vs (≤ 4.5

658 km/s) can be seen in the uppermost mantle beneath the Saharan metacraton region. Here, the slow Vs may

659 be related to magma upwelling beneath the Tibesti volcanic center and other nearby hotspots. The

660 uppermost mantle Vs is relatively fast (≥ 4.6 km/s) beneath the Rif-Tell Atlas mountain, Anti-Atlas Orogen,

661 and the Central African Belt.

662 Figure 11(d) shows the profile DD' which begins from the Madagascar Island, traverses the Indian

663 Ocean, Mozambique Basin, Zambezi Orogen, Congo craton, CVL, Benue Trough, and terminates near the

664 West African craton. A thin layer of slow Vs (≤ 3 km/s) is seen in the uppermost crust across the profile.

665 The region of southern Madagascar is underlain by Vs < 4 km/s at crustal depths. Fast Vs (≥ 4 km/s)

666 characterizes the Indian Ocean crust that thins into the Mozambique Basin at the edge of the continent.

667 Slow Vs extending to the depth of ~15 km at this location indicates the presence of thick sediment beneath

the continent-ocean passive margin. The Zambezi Orogen and Congo Basin are characterized by relatively slow Vs (≤ 3.5 km/s) in the mid-upper crust, while thick layers of fast Vs are obvious beneath the Congo Basin in the lower crust. Localized fast Vs is obvious beneath the northern part of Congo craton and Benue Trough in the mid-upper crust (~10–20 km depth). The Taoudeni Basin within the West African craton is characterized by relatively slow Vs (≤ 3.2 km/s), indicating sediment as thick as ~10 km trapped beneath a thin layer of fast Vs. The profile is underlain by a lower crust of fast Vs (≥ 4 km/s). The crust is relatively thin (≤ 30 km) beneath southern Madagascar, Indian Ocean, and southern CVL (e.g., Ojo et al., 2019), while the Moho depth at other locations along the profile is ~35–45 km. The uppermost mantle Vs is relatively slow (≤ 4.5 km/s) beneath the Indian Ocean, Zambezi Orogen, Congo Basin, CVL, and Taoudeni Basin, whereas faster Vs (≥ 4.6 km/s) is mainly seen beneath parts of the Congo and the West African craton. A relatively slow uppermost mantle Vs beneath Mt. Cameroon, the only active volcano along the CVL, may indicate the possibility of small-scale mantle upwelling as proposed by several authors (e.g., Adams et al., 2018). This is supported by the presence of localized fast Vs anomaly in the mid-lower crust beneath the region, which may be resulted from cooled mafic body intruded into the crust during magma transport and eruption (e.g., Ojo et al., 2018, 2019).

5 Discussion

5.1 Seismic Evidence for Cratonic Remnants within the Saharan Metacraton

One of the main achievements of this study is the ability to reliably image the lithospheric structures in aseismic regions with sparse broadband seismic stations in Africa (Figure 2). An important example of such a location is north-central Africa which plays host to the poorly imaged Saharan Metacraton. The term "Saharan Metacraton" was put forward by Abdelsalam et al. (2002) to indicate that the cratonic unit in this area has been partially destroyed and highly remobilized during the Neoproterozoic time and has since lost its characteristically cold, thick, and dense subcontinental lithospheric mantle (SCLM) during collisional processes. Three cratonic remnants (Murzuq, Al-Kufrah, and Chad) overlain by sedimentary basins and separated by topographic swells, including Hoggar, Tibesti Massif, and Darfur Dome has been suspected to exist in this region (e.g., Fezaa et al., 2010; Abdelsalam et al., 2011; Liégeois et al., 2013; Sobh et al., 2020). To find seismic evidence for the existence of these suspected cratonic remnants, we present four cross-sections of our 3D Vs model across the proposed boundary of the SMC in Figure 12 and several horizontal slices together with the crustal thickness map across the region in Figure S6.

Figure 12(a) shows a profile traversing the Cameroon Volcanic Line, the Chad Basin (overlying the Chad cratonic remnant), and terminating at the northern end of the Al-Kufrah Basin (overlying the Al-Kufrah cratonic remnant). In the upper crust, we find slow Vs (≤ 3 km/s) which persists to a depth of ~8 km beneath the Chad Basin, indicating the existence of thick sediment. The sediment is thinner (< 5 km) at

the southern edge of the Al-Kufrah basin and becomes thicker towards the northern edge (Figure 12a). Underlying the sediment are localized fast velocity anomalies (≥ 4 km/s) typical of cratonic remnants at a shallow depth (< 10 km) beneath the Al-Kufrah basin and deeper (> 10 km) beneath the Chad Basin. We interpret the observed localized fast Vs bodies as likely cratonic remnants from the metacratonization process (Abdelsalam et al., 2002). The uppermost mantle beneath the Chad Basin is characterized by relatively fast Vs (≥ 4.5 km/s), whereas the mantle Vs beneath the Al-Kufrah basin is relatively slow (≤ 4.5 km/s).
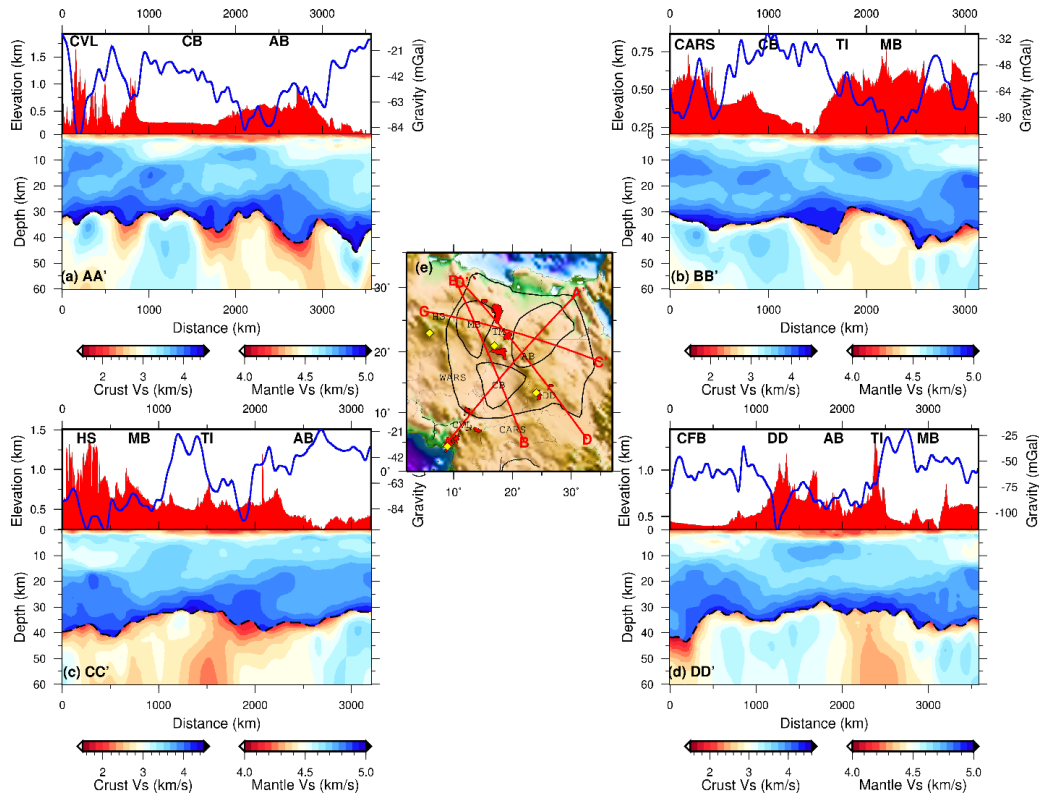

Figure 12. Cross-sections from the surface to 60-km depth along profiles (a) AA', (b) BB', (c) CC', and (d) DD'. (e) Map of study region showing locations of the profiles in (a-d) across the Saharan Metcraton, with black lines indicating the boundaries of the suspected cratonic remnants (Liégeois et al., 2013). Plotted on top of each cross-section is the elevation from ETOPO1 (Amante & Eakins, 2009) in red and the Bouguer gravity anomaly (EIGEN-6C4, Förste et al., 2014) profile in blue. The yellow diamonds in (e) mark locations of hotspots in the study region.

Profile BB' traverse the Central Africa Rift System (CARS) into the Chad and Murzuq basins and terminating outside the SCM (Figure 12b). Beneath this profile, the Murzuq basin is characterized by relatively thin sediment (~2 km) underlain by a localized fast Vs body in the uppermost crust and a slow Vs in the uppermost mantle.

In profile CC' (Figure 12c), slow Vs (≤ 3 km/s) persists down to ~15-km depth around the Hoggar hotspot on top of a thick layer of fast Vs and a slow upper mantle. Beneath the Murzuq and Al-Kufrah basins in Profile CC' (Figure 12c), the cratonic remnant is not obvious in the mid-lower crust, suggesting that the fast Vs body is limited to the southern part of the inferred boundaries. However, the underlying mantle Vs is relatively slow as observed in profile BB'. Relatively slow mantle Vs and less dense Bouguer gravity anomaly are found beneath the Tibesti hotspot underlain by obvious mantle upwelling (Figures 12c&d). Such an anomalously slow upper mantle Vs continues to a greater depth and has been observed in the global/continental-scale tomographic models (e.g., Fishwick, 2010; Schaeffer & Lebedev, 2013; Emry et al., 2019). This also agrees with the observation of Sobh et al. (2020) who found high temperatures related to mantle upwelling beneath the Tibesti hotspot. We also note that outside of the cratonic remnant and swells, the other parts of SMC are characterized by relatively fast upper mantle Vs.

In profile DD' (Figure 12d), localized fast Vs observed in profile AA' is also present at the southern edge of the Al-Kufrah basin underlain by a Vs of ~4.5 km/s in the uppermost mantle. The mantle upwelling beneath the Tibesti hotspot is also obvious in profile DD'. Comparing the three previously identified cratonic remnants, we find small negative Bouguer gravity anomaly (low density) and relatively fast uppermost mantle Vs beneath the Chad basin (Figures 12a&b), whereas larger negative Bouguer gravity anomaly (high density) and relatively slow uppermost mantle Vs are found beneath both the Murzuq and Al-Kufrah basins (Figures 12b&d). Likewise, the cratonic remnant beneath the Chad basin reveals more homogeneous velocity distribution within the inferred boundaries, while the structures differ in the southern (faster Vs) and northern (slower Vs) parts of the Murzuq and Al-Kufrah cratonic remnants (Figure S6). Sobh et al. (2020) observed that the Al-Kufrah cratonic remnant is characterized by higher density and lower temperature and is different from the Murzuq and Chad cratonic remnants. Based on our 3D model, a larger portion of the Al-Kufrah cratonic remnant in the north is characterized by slower Vs than the other two cratonic remnants, which is consistent with the observation of Sobh et al. (2020). We note that the three previously reported cratonic remnants are not located entirely within the boundaries inferred by Liégeois et al. (2013), as seen in the horizontal slices of our 3D Vs model in Figure 12(e). Rather, the geometry and locations of the fast Vs bodies that are best revealed by our model at mid-lower crustal depth (~25–40 km) indicate a northward offset (Figure 12e). Against the argument of Liégeois et al. (2005), we observe unique mantle upwellings beneath each of the intra-cratonic Cenozoic volcanic swells (i.e. Hoggar, Tibesti, and Darfur Dome), suggesting that they may be fed by unconnected plumes (Burke, 1996; Wilson & Guiraud, 1992; Sebai et al., 2006; Montagner et al., 2007).

Seismic estimates of the crustal thickness around the SMC are limited because of the sparsity of seismic station, and estimates from gravity modeling are subjected to high uncertainty due to trade-offs with mantle density anomalies (Herceg et al., 2016; Sobh et al., 2020). However, our new model reveals

that the crustal thicknesses in areas around and within the SMC range from ~28 to 52 km (Figure 12f). Thick crust (~40–45 km) is observed in the northern part of SMC encompassing the northern part of the Al-Kufrah basin whereas the western part of SMC is characterized by a crustal thickness of ~36 km. However, thin-crust (≤ 30km) underlies the south-central part of SMC including the southern part of the Murzuq and Al-Kufrah basins and the entire Chad basin. A circular region that encompasses the southern portion of the inferred cratonic remnant boundaries and most of the southwestern part of the Chad basin delineates the area of thin crust (≤ 32 km). This area is surrounded by a much thicker crust (~34–40 km) within the SMC (Figure 12f).

Previous studies suggested that the destruction of the interior of the former emplaced craton in the Sahara region can be attributed to several collisional events along its edges, including collisions with the Arabian-Nubian Shield to the east, the Tuareg Shield and West African Craton to the west, the Congo Craton to the south and an unnamed continent to the north. It has been hypothesized that the collisions probably led to the shortening (i.e. crustal thickening) and subsequent delamination of the sub-continental lithospheric mantle along zones of weakness within the craton, followed by high-temperature metamorphism as well as magma generation (Abdelsalam et al., 2002, 2011; Liégeois et al., 2005, 2013; Sobh et al., 2020). Results based on our 3D lithospheric model indicate that a combination of collisional events along the craton edges in addition to widespread Cenozoic volcanism may have contributed significantly to the metacratonization of the originally emplaced craton (Figures 12 and S6). This is evidenced by the emplacement of several localized fast Vs bodies within the SMC and the existence of thick crust around the SCM but the thin crust in the central-southern part of the remobilized craton (Figures 12e & f).

5.2 Secular Variation in Crustal Genesis

Knowledge about the nature of the Precambrian crust is important for developing geodynamic models of crustal genesis and evolution (Kachingwe et al., 2015). Since most parts of the African continent and Arabia are underlain by Precambrian crust (Milesi et al., 2010), several studies have tried to establish the relationship between crustal parameters and basement geologic age to advance our understanding of the formation and evolution of the continental crust. However, different results have been obtained by different research groups, leading to a continuing debate in the literature with some arguing for an obvious relationship (e.g., Durrheim & Mooney, 1991, 1994; Thompson et al., 2010; Abbott et al., 2013), while others claiming no discernible relation (e.g., Rudnick & Fountain, 1995; Al-Damegh et al., 2005; Kennett et al., 2011; Tugume et al., 2012, 2013; Stankiewicz & De Wit, 2013; Kachingwe et al., 2015).

To contribute to this important discussion, we compare the estimated crustal properties from this study to the age of the underlying basement rocks (e.g., Tugume et al., 2013). In Table 2, we list our estimated

789 thicknesses and average velocities in the upper, middle, lower, and whole crust as well as the thickness of
790 High-Velocity Layer (HVL) in the lower crust with respect to the ages of Archean and Proterozoic terranes
791 compiled by Tugume et al. (2013). We find variations in the crustal properties among and within individual
792 geological provinces that are related to the local geological settings. For example, in the Archean terrains,
793 thick fast velocity layers (> 10 km) underlain the North Limpopo Belt and Witwatersrand Terrane, whereas
794 other Archean provinces are underlain by relatively thin layers (< 5 km) characterized by much faster
795 velocity.

796 **Table 2.** Comparison between the estimated crustal properties from this study and the ages of underlying
797 rocks in southern and eastern Africa and the Arabian Shield from Tugume et al. (2013).

Longitude (°)	Latitude (°)	Location	Geologic Age	Crustal Thickness (km)	HVL Thickness (km)	Avg. Upper Crust (km/s)	Avg. Middle Crust (km/s)	Avg. Lower Crust (km/s)	Avg. Crustal Velocity (km/s)
33.3	-5.1	Dodoman Terrane	Archean	30.15	2.16	3.51	3.74	3.93	3.72
33.6	-2.4	Nyanzian Terrane	Archean	31.65	2.95	3.44	3.84	3.95	3.74
24.1	-21.4	Magondi Belt	Archean	34.01	2.17	3.42	3.72	3.91	3.68
28.2	-21	Central Limpopo Belt	Archean	34.55	3.47	3.52	3.83	3.95	3.76
14.7	2.8	Congo Craton	Archean	35	1.83	3.56	3.77	3.8	3.71
29.8	-18.3	East Towke Terrane	Archean	35.76	1.77	3.52	3.69	3.9	3.7
32.1	-20.9	South Limpopo Belt	Archean	37.91	2.49	3.52	3.77	3.98	3.75
26.4	-27.8	Witwaterstand Terrane	Archean	38.27	12.44	3.57	3.87	4.15	3.86
33.8	-18.8	North Limpopo Belt	Archean	39.07	11.74	3.38	3.74	4.08	3.74
24.7	-25.5	Kimberley Terrane	Archean	39.65	4.72	3.61	3.81	3.96	3.79
30.3	-25.9	Swaziland Terrane	Archean	41.51	1.45	3.57	3.92	3.96	3.81
30.9	-22.6	Pietersbug Terrane	Archean	44.37	1.51	3.57	3.91	3.83	3.77
		Average Archean		36.83 ± 3.92	4.06 ± 3.70	3.52 ± 0.07	3.80 ± 0.07	3.95 ± 0.09	3.75 ± 0.05
12.7	4.7	Oubanguide Belt	Proterozoic	29.7	2.05	3.47	3.85	3.84	3.72
25.6	-18	Okwa Terrane	Proterozoic	33.5	2.2	3.41	3.73	3.91	3.68
31.4	1.5	Rwenzori Belt	Proterozoic	33.77	0.81	3.43	3.66	3.67	3.59
21.8	-29.6	Namaqua Natal Belt	Proterozoic	33.9	2.52	3.57	3.76	3.89	3.74
30	-2.4	Kibaran Belt	Proterozoic	34.15	1.42	3.48	3.76	3.82	3.69
30.3	-5.2	Ubendian Belt	Proterozoic	34.64	2.01	3.49	3.77	3.88	3.71
43.3	24.3	Afif Terrane	Proterozoic	34.99	2.15	3.27	3.76	3.77	3.6
35.2	-7.6	Usagaran Belt	Proterozoic	35.34	4.92	3.48	3.71	4	3.73
41.2	20.9	Asir Terrane	Proterozoic	37.15	9.25	3.57	3.9	4	3.82
38.2	-1	Mozambique Belt	Proterozoic	37.23	11.64	3.43	3.77	4.22	3.8
43.9	19.8	Nabitah Terrane	Proterozoic	37.66	2.96	3.47	4.02	3.95	3.81
27.3	-19	West Tokwe Terrane	Proterozoic	37.87	7.94	3.5	3.73	4.06	3.76
45.2	22.3	Af Ryan Terrane	Proterozoic	38.23	5.02	3.29	3.78	3.99	3.69
22.6	-25.6	Kheis Province	Proterozoic	39.39	2.91	3.53	3.74	3.94	3.73
		Average Proterozoic		35.54 ± 2.46	4.13 ± 3.15	3.46 ± 0.09	3.78 ± 0.09	3.92 ± 0.13	3.72 ± 0.07

798
799

800 In the Archean terranes, the crust is thick (> 40 km) beneath the Swaziland and Pietersburg terranes
801 but thin (~30 km) beneath the Dodoman and Nyanzian terranes. Similarly, in the Proterozoic terranes, the
802 Oubanguides Belt and Okwa terranes are underlain by relatively thin crust (< 34 km), while thick crust (>
803 38 km) exists beneath the Af Ryan Terrane and Kheis Province. Variations of up to ~0.3 km/s in Vs are
804 seen among and within the Archean and Proterozoic terranes (Table 2). The average crustal thicknesses are
805 36.83 ± 3.92 km and 35.54 ± 2.46 km in the Achaean and Proterozoic terranes, respectively, indicating
806 similarity within the estimated uncertainties. Likewise, the mean thickness of HVL in the lower crust, which

807 could indicate compositional differences, is also similar (i.e. 4.06 ± 3.70 km beneath the Achaean terrain
808 and 4.13 ± 3.15 km beneath the Proterozoic terrain). The average velocity differences between the Archean
809 and Proterozoic terranes in the upper, mid, lower, and the entire crust are less than 0.1 km/s and also fall
810 within the estimated uncertainties. Therefore, we do not find an obvious relationship between the estimated
811 average crustal properties and the ages of the underlying basement rocks within the two terranes, in
812 agreement with some previous observations (e.g., Tugume et al., 2012, 2013; Kachingwe et al., 2015).
813 Previous authors with similar findings have indicated that this may be due to changes in the process that
814 formed the continental crust overtime or the crust in different provinces may have been significantly
815 modified by tectonic processes (e.g., lower crustal flow or foundering of eclogites into the mantle) such
816 that no discernible relations have been preserved (e.g., Rey et al., 2001; Zandt et al., 2004).

817

818 **6 Conclusions**

819 In this study, we use ambient seismic noise and earthquake data recorded by broadband seismic stations in
820 Africa, Europe, and Arabia for the past three decades to develop a new continental-scale 3D Vs model for
821 the African continent and the surrounding regions. The 3D Vs model shows slow Vs anomalies that coincide
822 with locations of thick sediments, zones of active deformation, and places where magma bodies are present
823 within the crust; while fast Vs regions correlate with cratonic units and thin oceanic crust (e.g., Pasyanos
824 & Nyblade, 2007). In the mid-lower crust, fast Vs reveals the geometry and locations of mafic bodies that
825 intruded into the crust and characterizes areas underlain by a relatively thin crust, while slow Vs is found
826 in regions underlain by thick crust and hotspots. Slow uppermost mantle Vs anomalies is seen beneath
827 mobile belts, hotspots, magma-assisted rift areas, and metacratons; while cratonic roots, mountain belts,
828 and basins are associated with fast Vs. The estimated crustal thickness in the study area range from ~20 to
829 55 km. The thickest crust is found beneath the cratons, whereas the thinnest crust is found in oceanic and
830 volcanic regions. We find thick layers of fast Vs in the lower crust around intra-cratonic basins, areas of
831 active rifting, continental margins, oceans as well as hotspot centers, and locations of diamond-rich
832 kimberlites/lamproites indicating the presence of mafic high-density materials. However, their formation
833 and/or removal mechanisms are controlled mainly by local tectonics in different parts of the study region.
834 Our tomography inversion achieved an unprecedented resolution in sparsely instrumented regions such
835 as north-central Africa where the poorly imaged Saharan Metacraton (SMC) is located. As a result, we
836 provide the first seismic evidence that confirms the existence of three suspected cratonic remnants (Murzuq,
837 Al-Kufrah, and Chad remnants) buried beneath thick sediments within the SMC and constrains their
838 locations and geometry. We also imaged distinct mantle upwelling beneath Hoggar, Tibesti Massif, and
839 Darfur Dome hotspots that they may be fed by unconnected plumes. The anomalies in our 3D Vs model
840 shows a better correlation with known tectonic features in the upper crust than the existing continental-

841 scale models (e.g., Laske et al., 2013). At uppermost mantle depths, our model is consistent with the existing

842 continental-scale and global models within the estimated uncertainties (e.g., Schaeffer & Lebedev, 2013;

843 Moulik & Ekstrom, 2014; Celli et al., 2020). Our new improved model can improve earthquake detection

844 and location in Africa that can lead to much better performance in the monitoring practice of the

845 Comprehensive Nuclear-Test-Ban Treaty. Our results are also useful for regional seismic hazard analysis

846 and geodynamic modeling studies. We make the model publicly available and hope to continue updating it

847 as time and funding allow.

848

861

862 **References**

863 Abbott, D. H., Mooney, W. D., & VanTongeren, J. A. (2013). The character of the Moho and lower crust within
864   Archean cratons and the tectonic implications. *Tectonophysics*, 609, 690-705.

865 Abdelsalam, M., Gao, S., & Liégeois, J. (2011). Upper mantle structure of the Saharan Metacraton. *Journal of*
866   *African Earth Sciences*, *60*(5), 328-336. doi: 10.1016/j.jafrearsci.2011.03.009

867 Abdelsalam, M., Liégeois, J., & Stern, R. (2002). The Saharan Metacraton. *Journal of African Earth*
868   *Sciences*, *34*(3-4), 119-136. doi: 10.1016/s0899-5362(02)00013-1

869 Accardo, N., Gaherty, J., Shillington, D., Ebinger, C., Nyblade, A., & Mbogoni, G. et al. (2017). Surface wave
870   imaging of the weakly extended Malawi Rift from ambient-noise and teleseismic Rayleigh waves from
871   onshore and lake-bottom seismometers. *Geophysical Journal International*, *209*(3), 1892-1905. doi:
872   10.1093/gji/ggx133

873 Accardo, N., Gaherty, J., Shillington, D., Hopper, E., Nyblade, A., & Ebinger, C. et al. (2020). Thermochemical
874   Modification of the Upper Mantle Beneath the Northern Malawi Rift Constrained From Shear Velocity
875   Imaging. *Geochemistry, Geophysics, Geosystems*, *21*(6). doi: 10.1029/2019gc008843

876   Adams, A., Miller, J., & Accardo, N. (2018). Relationships Between Lithospheric Structures and Rifting in the
877   East African Rift System: A Rayleigh Wave Tomography Study. *Geochemistry, Geophysics,*
878   *Geosystems*, *19*(10), 3793-3810. doi: 10.1029/2018gc007750

879   Adams, A., Nyblade, A., & Weeraratne, D. (2012). Upper mantle shear wave velocity structure beneath the East
880   African plateau: evidence for a deep, plateauwide low velocity anomaly. *Geophysical Journal*
881   *International*, *189*(1), 123-142. doi: 10.1111/j.1365-246x.2012.05373.x

882   Adimah, N., & Padhy, S. (2019). Ambient noise Rayleigh wave tomography across the Madagascar
883   island. *Geophysical Journal International*, *220*(3), 1657-1676. doi: 10.1093/gji/ggz542

884   Agius, M., & Lebedev, S. (2013). Tibetan and Indian lithospheres in the upper mantle beneath Tibet: Evidence
885   from broadband surface-wave dispersion. *Geochemistry, Geophysics, Geosystems*, *14*(10), 4260-4281. doi:
886   10.1002/ggge.20274

887   Aki, K., & Richards, P. G. (2002). *Quantitative seismology*.

888   Albaric, J., Deverchere, J., Perrot, J., Jakovlev, A., & Deschamps, A. (2014). Deep crustal earthquakes in North
889   Tanzania, East Africa: Interplay between tectonic and magmatic processes in an incipient
890   rift. *Geochemistry, Geophysics, Geosystems*, *15*(2), 374-394.

891   Al-Damegh, K., Sandvol, E., & Barazangi, M. (2005). Crustal structure of the Arabian plate: new constraints
892   from the analysis of teleseismic receiver functions. *Earth and Planetary Science Letters*, 231(3-4), 177-
893   196.

894   Amante, C., & Eakins, B. W. (2009). ETOPO1 arc-minute global relief model: procedures, data sources and
895   analysis.

896   Aster, R. C., Borchers, B., & Thurber, C. H. (2018). Parameter estimation and inverse problems. Elsevier.

897   Ayarza, P., Alvarez-Lobato, F., Teixell, A., Arboleya, M. L., Teson, E., Julivert, M., & Charroud, M. (2005).
898   Crustal structure under the central High Atlas Mountains (Morocco) from geological and gravity
899   data. *Tectonophysics*, *400*(1-4), 67-84.

900   Bagley, B., & Nyblade, A. A. (2013). Seismic anisotropy in eastern Africa, mantle flow, and the African
901   superplume. *Geophysical Research Letters*, *40*(8), 1500-1505.

902   Bailey, D. K. (1992). Episodic alkaline igneous activity across Africa: Implications for the causes of continental
903   break-up.   Geological   Society,London,   Special   Publications,   68(1),   91–98.
904   https://doi.org/10.1144/GSL.SP.1992.068.01.06

905   Bastow, I. D., Nyblade, A. A., Stuart, G. W., Rooney, T. O., & Benoit, M. H. (2008). Upper mantle seismic
906   structure beneath the Ethiopian hot spot: Rifting at the edge of the African low-velocity
907   anomaly. *Geochemistry, Geophysics, Geosystems*, *9*(12).

908   Begg, G. C., Griffin, W. L., Natapov, L. M., O'Reilly, S. Y., Grand, S. P., O'Neill, C. J., ... & Bowden, P. (2009).
909   The lithospheric architecture of Africa: Seismic tomography, mantle petrology, and tectonic
910   evolution. *Geosphere*, *5*(1), 23-50.

911   Benoit, M. H., Nyblade, A. A., Owens, T. J., & Stuart, G. (2006). Mantle transition zone structure and upper
912   mantle S velocity variations beneath Ethiopia: Evidence for a broad, deep-seated thermal
913   anomaly. *Geochemistry, Geophysics, Geosystems*, *7*(11).

914   Bensen, G. D., Ritzwoller, M. H., Barmin, M. P., Levshin, A. L., Lin, F., Moschetti, M. P., ... & Yang, Y. (2007).
915   Processing seismic ambient noise data to obtain reliable broad-band surface wave dispersion
916   measurements. *Geophysical Journal International*, *169*(3), 1239-1260.

917   Boschi, L., & Ekström, G. (2002). New images of the Earth's upper mantle from measurements of surface wave
918   phase velocity anomalies. *Journal of Geophysical Research: Solid Earth*, *107*(B4), ESE-1.

919 Bosworth, W., Huchon, P., & McClay, K. (2005). The red sea and gulf of aden basins. *Journal of African Earth*
920 *Sciences*, *43*(1-3), 334-378.

921 Brocher, T. M. (2005). Empirical relations between elastic wavespeeds and density in the Earth's crust. *Bulletin*
922 *of the seismological Society of America*, *95*(6), 2081-2092.

923 Brown, C., & Girdler, R. W. (1980). Interpretation of African gravity and its implication for the breakup of the
924 continents. *Journal of Geophysical Research: Solid Earth*, *85*(B11), 6443-6455.

925 Burke, K. (1996), The African plate, S. Afr. J. Geol., 99, 339–410.

926 Butcher, L. A., K. H. Mahan, and J. M. Allaz (2017), Late Cretaceous to Paleocene crustal hydration in the
927 Colorado Plateau, USA, from xenolith petrology and monazite geochronology, Lithosphere, 9,
928 doi:10.1130/L583.1.

929 Čadek, O., & Martinec, Z. (1991). Spherical harmonic expansion of the Earth's crustal thickness up to degree
930 and order 30. *Studia Geophysica et Geodaetica*, *35*(3), 151-165.

931 Cahen, L., Snelling, N., Delhal, J., & Vail, J. (1984). The geochronology and evolution of Africa. Oxford:
932 Clarendon Press.

933 Campillo, M., & Paul, A. (2003). Long-range correlations in the diffuse seismic coda. *Science*, *299*(5606), 547-
934 549.

935 Celli, N. L., Lebedev, S., Schaeffer, A. J., & Gaina, C. (2020). African cratonic lithosphere carved by mantle
936 plumes. *Nature communications*, *11*(1), 1-10.

937 Chambers, E. L., Harmon, N., Keir, D., & Rychert, C. A. (2019). Using ambient noise to image the northern
938 East African Rift. *Geochemistry, Geophysics, Geosystems*, *20*(4), 2091-2109.

939 Chen, H., Zhu, L., Wang, Q., Zhang, P., & Yang, Y. (2014). S-wave velocity structure of the North China from
940 inversion of Rayleigh wave phase velocity. *Journal of Asian Earth Sciences*, *88*, 178-191. doi:
941 10.1016/j.jseaes.2014.03.006

942 Chesler, R. (2012), The Geochemistry and Geochronology of Tanzanian Kimberlites, School of Earth Sci., The
943 Univ. of Melbourne, Melbourne.

944 Chevrot, S., & Zhao, L. (2007). Multiscale finite-frequency Rayleigh wave tomography of the Kaapvaal craton,
945 *Geophysical Journal International*, 169, 201-215, doi:10.1111/j.1365-246X.2006.03289.x.

946 Chorowicz, J. (2005), The East African Rift System, *J. Afr. Earth Sci.*, 43, 379–410.

947 Christensen, N. I., & Mooney, W. D. (1995). Seismic velocity structure and composition of the continental crust:
948 A global view. *Journal of Geophysical Research: Solid Earth*, *100*(B6), 9761-9788.

949 Civiero, C., Goes, S., Hammond, J. O., Fishwick, S., Ahmed, A., Ayele, A., ... & Leroy, S. (2016). Small-scale
950 thermal upwellings under the northern East African Rift from S travel time tomography. *Journal of*
951 *Geophysical Research: Solid Earth*, *121*(10), 7395-7408.

952 Coffin, M. F., & Rabinowitz, P. D. (1987). Reconstruction of Madagascar and Africa: evidence from the Davie
953 fracture zone and western Somali basin. *Journal of Geophysical Research: Solid Earth*, *92*(B9), 9385-9406.

954 Collins, A. (2006). Madagascar and the amalgamation of Central Gondwana. *Gondwana Research*, *9*(1-2), 3-
955 16. doi: 10.1016/j.gr.2005.10.001

956 Condie, K. C., Archean andesites, in Andesites, edited by R. S. Thorpe, p. 575 – 590, John Wiley, NY, 1982.

957 Cornell, D. H., Thomas, R. J., Gibson, R., Moen, H. F. G., Reid, D. L., Moore, J. M., & Gibson, R. L. (2006).
958 The Namaqua-Natal Province. Geological Society of South Africa.

959 Craig, T. J., Jackson, J. A., Priestley, K., & McKenzie, D. (2011). Earthquake distribution patterns in Africa:
960 their relationship to variations in lithospheric and geological structure, and their rheological
961 implications. *Geophysical Journal International*, *185*(1), 403-434.

Crosby, A. G., Fishwick, S., & White, N. (2010). Structure and evolution of the intracratonic Congo Basin. *Geochemistry, Geophysics, Geosystems*, *11*(6).

de Vos, D., Paulssen, H., & Fichtner, A. (2013). Finite-frequency sensitivity kernels for two-station surface wave measurements. *Geophysical Journal International*, *194*(2), 1042-1049.

De Wit, M. J., de Ronde, C. E., Tredoux, M., Roering, C., Hart, R. J., Armstrong, R. A., ... & Hart, R. A. (1992). Formation of an Archaean continent. *Nature*, *357*(6379), 553-562.

de Wit, M. J. (2003). Madagascar: Heads it's a continent, tails it's an island, Annu. Rev. Earth Planet. Sci., 31(1), 213–248.

Deen, T. J., Griffin, W. L., Begg, G., O'Reilly, S. Y., Natapov, L. M., & Hronsky, J. (2006). Thermal and compositional structure of the subcontinental lithospheric mantle: Derivation from shear wave seismic tomography. *Geochemistry, Geophysics, Geosystems*, *7*(7).

Domingues, A., Silveira, G., Ferreira, A. M., Chang, S. J., Custódio, S., & Fonseca, J. F. (2016). Ambient noise tomography of the East African Rift in Mozambique. *Geophysical Journal International*, *204*(3), 1565-1578.

Dorbath, C., Dorbath, L., Fairhead, J. D., & Stuart, G. W. (1986). A teleseismic delay time study across the Central African Shear Zone in the Adamawa region of Cameroon, West Africa. *Geophysical Journal International*, *86*(3), 751-766.

Ducea, M., & Saleeby, J. (1998). A case for delamination of the deep batholithic crust beneath the Sierra Nevada, California. *International Geology Review*, *40*(1), 78-93.

Durrheim, R. J., & Nyblade, A. A. (2019). AfricaArray studies of the lithosphere in sub-Saharan Africa. *Acta Geologica Sinica-English Edition*, *93*, 22-24.

Durrheim, R. (2008). Africa Array. Quest, 4(2), 14-15.

Durrheim, R. J., & Mooney, W. D. (1991). Archean and Proterozoic crustal evolution: Evidence from crustal seismology. *Geology*, 19(6), 606-609.

Durrheim, R. J., & Mooney, W. D. (1994). Evolution of the Precambrian lithosphere: seismological and geochemical constraints. *Journal of Geophysical Research: Solid Earth*, 99(B8), 15359-15374.

Ebinger, C. (2005). Continental break-up: the East African perspective. *Astronomy & Geophysics*, *46*(2), 2-16.

Ebinger, C. J. (1989). Tectonic development of the western branch of the East African rift system. *Geological Society of America Bulletin*, *101*(7), 885-903.

Ebinger, C. J., & Sleep, N. H. (1998). Cenozoic magmatism throughout east Africa resulting from impact of a single plume. *Nature*, *395*(6704), 788-791.

Ebinger, C. J., Deino, A. L., Drake, R. E., & Tesha, A. L. (1989). Chronology of volcanism and rift basin propagation: Rungwe volcanic province, East Africa. *Journal of Geophysical Research: Solid Earth*, *94*(B11), 15785-15803.

Ebinger, C. J., Oliva, S. J., Pham, T. Q., Peterson, K., Chindandali, P., Illsley-Kemp, F., ... & Gaherty, J. (2019). Kinematics of active deformation in the Malawi Rift and Rungwe Volcanic Province, Africa. *Geochemistry, Geophysics, Geosystems*, *20*(8), 3928-3951.

Eglington, B. M., & Armstrong, R. A. (2004). The Kaapvaal Craton and adjacent orogens, southern Africa: a geochronological database and overview of the geological development of the craton. *South African Journal of Geology*, *107*(1-2), 13-32.

Emry, E. L., Shen, Y., Nyblade, A. A., Flinders, A., & Bao, X. (2019). Upper mantle earth structure in Africa from full-wave ambient noise tomography. *Geochemistry, Geophysics, Geosystems*, *20*(1), 120-147.

1004 Endrun, B., Lebedev, S., Meier, T., Tirel, C., & Friederich, W. (2011). Complex layered deformation within the
1005   Aegean crust and mantle revealed by seismic anisotropy. *Nature Geoscience*, *4*(3), 203-207.

1006 Erdman, M. E., Lee, C. T. A., Levander, A., & Jiang, H. (2016). Role of arc magmatism and lower crustal
1007   foundering in controlling elevation history of the Nevadaplano and Colorado Plateau: A case study of
1008   pyroxenitic lower crust from central Arizona, USA. *Earth and Planetary Science Letters*, *439*, 48-57.

1009 Faccenna, C., Becker, T. W., Lucente, F. P., Jolivet, L., & Rossetti, F. (2001). History of subduction and back
1010   arc extension in the Central Mediterranean. *Geophysical Journal International*, *145*(3), 809-820.

1011 Faccenna, C., Piromallo, C., Crespo-Blanc, A., Jolivet, L., & Rossetti, F. (2004). Lateral slab deformation and
1012   the origin of the western Mediterranean arcs. *Tectonics*, *23*(1).

1013 Fadel, I., van der Meijde, M., & Paulssen, H. (2018). Crustal structure and dynamics of Botswana. *Journal of
1014   Geophysical Research: Solid Earth*, *123*(12), 10-659.

1015 Fagereng, Å. (2013). Fault segmentation, deep rift earthquakes and crustal rheology: Insights from the 2009
1016   Karonga sequence and seismicity in the Rukwa–Malawi rift zone. *Tectonophysics*, *601*, 216-225.

1017 Fairhead, J. D., & Okereke, C. S. (1988). Depths to major density contrats beneath the West African rift system
1018   in Nigeria and Cameroon based on the spectral analysis of gravity data. *Journal of African Earth Sciences
1019   (and the Middle East)*, *7*(5-6), 769-777.

1020 Fang, H., Zhang, H., Yao, H., Allam, A., Zigone, D., Ben-Zion, Y., ... & van der Hilst, R. D. (2016). A new
1021   algorithm for three-dimensional joint inversion of body wave and surface wave data and its application to
1022   the Southern California plate boundary region. *Journal of Geophysical Research: Solid Earth*, *121*(5),
1023   3557-3569.

1024 Faure, S., Godey, S., Fallara, F., & Trépanier, S. (2011). Seismic architecture of the Archean North American
1025   mantle and its relationship to diamondiferous kimberlite fields. *Economic Geology*, *106*(2), 223-240.

1026 Fezaa, N., Liégeois, J. P., Abdallah, N., Cherfouh, E. H., De Waele, B., Bruguier, O., & Ouabadi, A. (2010).
1027   Late Ediacaran geological evolution (575–555 Ma) of the Djanet Terrane, Eastern Hoggar, Algeria,
1028   evidence for a Murzukian intracontinental episode. *Precambrian Research*, *180*(3-4), 299-327.

1029 Fischer, K. M. (2002), Waning buoyancy in the crustal roots of old mountains, Nature, 417, 933–936.

1030 Fishwick, S. (2010). Surface wave tomography: Imaging of the lithosphere–asthenosphere boundary beneath
1031   central and southern Africa?. *Lithos*, *120*(1-2), 63-73. doi: 10.1016/j.lithos.2010.05.011

1032 Fishwick, S., & Bastow, I. D. (2011). Towards a better understanding of African topography: a review of passive-
1033   source seismic studies of the African crust and upper mantle. *Geological Society, London, Special
1034   Publications*, *357*(1), 343-371.

1035 Fitton, J., & Dunlop, H. (1985). The Cameroon line, West Africa, and its bearing on the origin of oceanic and
1036   continental alkali basalt. *Earth and Planetary Science Letters*, *72*(1), 23-38. doi: 10.1016/0012-
1037   821x(85)90114-1

1038 Forte, A. M., Moucha, R., Simmons, N. A., Grand, S. P., Rowley, D. B., & Mitrovica, J. (2010). New Insights
1039   into the Basin and Swell Dynamics of Africa Driven by Whole-Mantle Convection. *AGUFM*, *2010*, T23F-
1040   06.

1041 Foster, K., Dueker, K., Schmandt, B., & Yuan, H. (2014). A sharp cratonic lithosphere–asthenosphere boundary
1042   beneath the American Midwest and its relation to mantle flow. *Earth and Planetary Science Letters*, *402*,
1043   82-89.

1044 Frizon de Lamotte, D., Saint Bezar, B., Bracène, R., & Mercier, E. (2000). The two main steps of the Atlas
1045   building and geodynamics of the western Mediterranean. *Tectonics*, *19*(4), 740-761.

1046 Funck, T., Louden, K. E., & Reid, I. D. (2001). Crustal structure of the Grenville Province in southeastern
1047   Labrador from refraction seismic data: evidence for a high-velocity lower crustal wedge. *Canadian Journal*
1048   *of Earth Sciences*, *38*(10), 1463-1478.

1049 Furman, T., Bryce, J. G., Karson, J., & Iotti, A. (2004). East African Rift System (EARS) plume structure:
1050   insights from Quaternary mafic lavas of Turkana, Kenya. *Journal of Petrology*, *45*(5), 1069-1088.

1051 George, R., Rogers, N., & Kelley, S. (1998). Earliest magmatism in Ethiopia: evidence for two mantle plumes
1052   in one flood basalt province. *Geology*, *26*(10), 923-926.

1053 Globig, J., Fernàndez, M., Torne, M., Vergés, J., Robert, A., & Faccenna, C. (2016). New insights into the crust
1054   and lithospheric mantle structure of Africa from elevation, geoid, and thermal analysis. *Journal of*
1055   *Geophysical Research: Solid Earth*, *121*(7), 5389-5424.

1056 Goldstein, P., Dodge, D., Firpo, M., Minner, L., Lee, W. H. K., Kanamori, H., ... & Kisslinger, C. (2003).
1057   SAC2000: Signal processing and analysis tools for seismologists and engineers. The IASPEI international
1058   handbook of earthquake and engineering seismology, 81, 1613-1620.

1059 Grand, S. P. (2002). Mantle shear–wave tomography and the fate of subducted slabs. *Philosophical Transactions*
1060   *of the Royal Society of London. Series A: Mathematical, Physical and Engineering Sciences*, *360*(1800),
1061   2475-2491.

1062 Grand, S. P., Van der Hilst, R. D., & Widiyantoro, S. (1997). High resolution global tomography: a snapshot of
1063   convection in the Earth. *Geological Society of America Today*, *7*(4).

1064 Guiraud, R., & Maurin, J. C. (1992). Early Cretaceous rifts of Western and Central Africa: an
1065   overview. *Tectonophysics*, *213*(1-2), 153-168.

1066 Gurnis, M., Mitrovica, J. X., Ritsema, J., & van Heijst, H. J. (2000). Constraining mantle density structure using
1067   geological evidence of surface uplift rates: The case of the African superplume. *Geochemistry, Geophysics,*
1068   *Geosystems*, *1*(7).

1069 Hansen, S. E., & Nyblade, A. A. (2013). The deep seismic structure of the Ethiopia/Afar hotspot and the African
1070   superplume. *Geophysical Journal International*, *194*(1), 118-124.

1071 Hansen, S. E., Nyblade, A. A., Julia, J., Dirks, P. H., & Durrheim, R. J. (2009). Upper-mantle low-velocity zone
1072   structure beneath the Kaapvaal craton from S-wave receiver functions. *Geophysical Journal*
1073   *International*, *178*(2), 1021-1027.

1074 Hassan, R., Williams, S., Gurnis, M., & Müller, D. (2020). East African topography and volcanism explained
1075   by a single, migrating plume. *Geoscience Frontiers*. doi: 10.1016/j.gsf.2020.01.003

1076 Herceg, M., Artemieva, I. M., & Thybo, H. (2016). Sensitivity analysis of crustal correction for calculation of
1077   lithospheric mantle density from gravity data. *Geophysical Journal International*, *204*(2), 687-696.

1078 Herrmann, R. B. (2013). Computer programs in seismology: An evolving tool for instruction and
1079   research. *Seismological Research Letters*, *84*(6), 1081-1088.

1080 Herrmann, R. B., & Ammon, C. J. (2004). Surface waves, receiver functions and crustal structure. *Computer*
1081   *programs in seismology, version*, *3*, 30.

1082 Hilton, D. R., Halldórsson, S. A., Barry, P. H., Fischer, T. P., de Moor, J. M., Ramirez, C. J., ... & Scarsi, P.
1083   (2011). Helium isotopes at Rungwe Volcanic Province, Tanzania, and the origin of East African
1084   plateaux. *Geophysical Research Letters*, *38*(21).

1085 Hopper, E., Gaherty, J. B., Shillington, D. J., Accardo, N. J., Nyblade, A. A., Holtzman, B. K., ... & Mulibo, G.
1086   D. (2020). Preferential localized thinning of lithospheric mantle in the melt-poor Malawi Rift. *Nature*
1087   *Geoscience*, 1-6.

1088   Huang, Z., Wang, P., Zhao, D., Wang, L., & Xu, M. (2014). Three-dimensional P wave azimuthal anisotropy in
1089   the lithosphere beneath China. *Journal of Geophysical Research: Solid Earth*, *119*(7), 5686-5712.

1090   Humphreys, E., & Clayton, R. W. (1988). Adaptation of back projection tomography to seismic travel time
1091   problems. *Journal of Geophysical Research: Solid Earth*, *93*(B2), 1073-1085.

1092   Inoue, H., Fukao, Y., Tanabe, K., & Ogata, Y. (1990). Whole mantle P-wave travel time tomography. *Physics
1093   of the Earth and Planetary Interiors*, *59*(4), 294-328.

1094   Jackson, J., & Blenkinsop, T. (1993). The Malaŵi earthquake of March 10, 1989: Deep faulting within the East
1095   African rift system. *Tectonics*, *12*(5), 1131-1139.

1096   Jelsma, H. A., & Dirks, P. H. (2002). Neoarchaean tectonic evolution of the Zimbabwe Craton. *Geological
1097   Society, London, Special Publications*, *199*(1), 183-211.

1098   Johnson, M. R., Anhauesser, C. R., & Thomas, R. J. (2006). The Geology of South Africa. Geological Society
1099   of South Africa.

1100   Jones, C. H., Mahan, K. H., Butcher, L. A., Levandowski, W. B., & Farmer, G. L. (2015). Continental uplift
1101   through crustal hydration. Geology, 43(4), 355–358. https://doi.org/10.1130/G36509.1

1102   Kachingwe, M., Nyblade, A., & Julia, J. (2015). Crustal structure of Precambrian terranes in the southern African
1103   subcontinent with implications for secular variation in crustal genesis. Geophysical Journal International,
1104   202(1), 533-547.

1105   Kadima, E., Delvaux, D., Sebagenzi, S. N., Tack, L., & Kabeya, S. M. (2011). Structure and geological history
1106   of the Congo Basin: an integrated interpretation of gravity, magnetic and reflection seismic data. *Basin
1107   Research*, *23*(5), 499-527.

1108   Kanamori, H., & Anderson, D. L. (1977). Importance of physical dispersion in surface wave and free oscillation
1109   problems. *Reviews of Geophysics*, *15*(1), 105-112.

1110   Kästle, E. D., El-Sharkawy, A., Boschi, L., Meier, T., Rosenberg, C., Bellahsen, N., ... & Weidle, C. (2018).
1111   Surface wave tomography of the Alps using ambient-noise and earthquake phase velocity
1112   measurements. *Journal of Geophysical Research: Solid Earth*, *123*(2), 1770-1792.

1113   Kästle, E. D., Soomro, R., Weemstra, C., Boschi, L., & Meier, T. (2016). Two-receiver measurements of phase
1114   velocity: cross-validation of ambient-noise and earthquake-based observations. *Geophysical Journal
1115   International*, *207*(3), 1493-1512.

1116   Kaviani, A., Paul, A., Moradi, A., Mai, P. M., Pilia, S., Boschi, L., ... & Sandvol, E. (2020). Crustal and
1117   uppermost mantle shear wave velocity structure beneath the Middle East from surface wave
1118   tomography. *Geophysical Journal International*, *221*(2), 1349-1365.

1119   Kennett, B. L. N., Sambridge, M. S., & Williamson, P. R. (1988). Subspace methods for large inverse problems
1120   with multiple parameter classes. *Geophysical Journal International*, *94*(2), 237-247.

1121   Kennett, B. L., Engdahl, E. R., & Buland, R. (1995). Constraints on seismic velocities in the Earth from
1122   traveltimes. Geophysical Journal International, 122(1), 108-124.

1123   Kennett, B. L. N., Salmon, M., Saygin, E., & Group, A. W. (2011). AusMoho: the variation of Moho depth in
1124   Australia. Geophysical Journal International, 187(2), 946-958.

1125   Kgaswane, E. M., Nyblade, A. A., Julià, J., Dirks, P. H., Durrheim, R. J., & Pasyanos, M. E. (2009). Shear wave
1126   velocity structure of the lower crust in southern Africa: Evidence for compositional heterogeneity within
1127   Archaean and Proterozoic terrains. *Journal of Geophysical Research: solid earth*, *114*(B12).

1128   Kieffer, B., Arndt, N., Lapierre, H., Bastien, F., Bosch, D., Pecher, A., ... & Keller, F. (2004). Flood and shield
1129   basalts from Ethiopia: magmas from the African superswell. *Journal of Petrology*, *45*(4), 793-834.

1130 Kind, R., Yuan, X., Saul, J., Nelson, D., Sobolev, S. V., Mechie, J., ... & Jiang, M. (2002). Seismic images of
1131   crust and upper mantle beneath Tibet: evidence for Eurasian plate subduction. *science*, *298*(5596), 1219-
1132   1221.

1133 King, S. D. (2007). Hotspots and edge-driven convection. *Geology*, *35*(3), 223-226.

1134 King, S. D., & Anderson, D. L. (1995). An alternative mechanism of flood basalt formation. *Earth and Planetary*
1135   *Science Letters*, *136*(3-4), 269-279.

1136 King, S. D., & Anderson, D. L. (1998). Edge-driven convection. *Earth and Planetary Science Letters*, *160*(3-4),
1137   289-296.

1138 King, S. D., & Ritsema, J. (2000). African hot spot volcanism: small-scale convection in the upper mantle
1139   beneath cratons. *Science*, *290*(5494), 1137-1140.

1140 Kramers, J. D., S. McCourt, and D. D. van Reenen (2006), The Limpopo Belt, in The Geology of South Africa,
1141   edited by M. R. Johnson, C. R. Anhaeusser, and R. J. Thomas, pp. 209 – 236, Geol. Soc. of S. Afr.,
1142   Johannesburg, South Africa.

1143 Kusky, T. M., Windley, B. F., & Zhai, M. G. (2007). Lithospheric thinning in eastern Asia; constraints, evolution,
1144   and tests of models. *Geological Society, London, Special Publications*, *280*(1), 331-343.

1145 Laó-Dávila, D. A., Al-Salmi, H. S., Abdelsalam, M. G., & Atekwana, E. A. (2015). Hierarchical segmentation
1146   of the Malawi Rift: The influence of inherited lithospheric heterogeneity and kinematics in the evolution of
1147   continental rifts. *Tectonics*, *34*(12), 2399-2417.

1148 Laske, G. & Masters, G. (1997). A Global Digital Map of Sediment Thickness, *EOS Trans. AGU*, 78, F483.

1149 Laske, G., Masters, G., Ma, Z., & Pasyanos, M. (2013). Update on CRUST1. 0—A 1-degree global model of
1150   Earth's crust. In *Geophys. Res. Abstr* (Vol. 15, p. 2658).

1151 Lavayssière, A., Rychert, C., Harmon, N., Keir, D., Hammond, J. O., Kendall, J. M., ... & Leroy, S. (2018).
1152   Imaging lithospheric discontinuities beneath the Northern East African Rift using S-to-P receiver
1153   functions. *Geochemistry, Geophysics, Geosystems*, *19*(10), 4048-4062.

1154 Lebedev, S., Boonen, J., & Trampert, J. (2009). Seismic structure of Precambrian lithosphere: new constraints
1155   from broad-band surface-wave dispersion. *Lithos*, *109*(1-2), 96-111.

1156 Legendre, C., Zhao, L., & Chen, Q.-f. (2015). Upper-mantle shear-wave structure under East and Southeast Asia
1157   from Automated Multimode Inversion of Waveforms, *Geophysical Journal International*, 203, 707-719.

1158 Lekić, V., Panning, M., & Romanowicz, B. (2010). A simple method for improving crustal corrections in
1159   waveform tomography. *Geophysical Journal International*, *182*(1), 265-278.

1160 Lévěque, J. J., Rivera, L., & Wittlinger, G. (1993). On the use of the checker-board test to assess the resolution
1161   of tomographic inversions. *Geophysical Journal International*, *115*(1), 313-318.

1162 Li, H., Su, W., Wang, C. Y., & Huang, Z. (2009). Ambient noise Rayleigh wave tomography in western Sichuan
1163   and eastern Tibet. *Earth and Planetary Science Letters*, *282*(1-4), 201-211.

1164 Liégeois, J., Benhallou, A., Azzouni-Sekkal, A., Yahiaoui, R., & Bonin, B. (2005). The Hoggar swell and
1165   volcanism: reactivation of the Precambrian Tuareg shield during Alpine convergence and West African
1166   Cenozoic volcanism. *SPECIAL PAPERS-GEOLOGICAL SOCIETY OF AMERICA*, *388*, 379.

1167 Liégeois, J.-P., Abdelsalam, M. G., Ennih, N., & Ouabadi, A. (2013). Metacraton: Nature, genesis and behavior.
1168   *Gondwana Research*, 23(1), 220–237. https://doi.org/10.1016/j.gr.2012.02.016

1169 Lin, F. C., Moschetti, M. P., & Ritzwoller, M. H. (2008). Surface wave tomography of the western United States
1170   from ambient seismic noise: Rayleigh and Love wave phase velocity maps. *Geophysical Journal*
1171   *International*, *173*(1), 281-298.

Lithgow-Bertelloni, C., & Silver, P. G. (1998). Dynamic topography, plate driving forces and the African superswell. *Nature*, *395*(6699), 269-272.

Lu, Y., Stehly, L., Paul, A., & AlpArray Working Group. (2018). High-resolution surface wave tomography of the European crust and uppermost mantle from ambient seismic noise. *Geophysical Journal International*, *214*(2), 1136-1150.

Lucassen, F., Franz, G., Romer, R. L., & Dulski, P. (2008). Late Cenozoic xenoliths as a guide to the chemical–isotopic composition and thermal state of the upper mantle under northeast Africa. *European Journal of Mineralogy*, *20*(6), 1079-1096.

Luo, Y., Yang, Y., Xu, Y., Xu, H., Zhao, K., & Wang, K. (2015). On the limitations of interstation distances in ambient noise tomography. *Geophysical Journal International*, *201*(2), 652-661.

Ma, Z., & Masters, G. (2014). A new global Rayleigh-and Love-wave group velocity dataset for constraining lithosphere properties. *Bulletin of the Seismological Society of America*, *104*(4), 2007-2026.

MacGregor, L. M., Constable, S., & Sinha, M. C. (1998). The RAMESSES experiment—III. Controlled-source electromagnetic sounding of the Reykjanes Ridge at 57° 45′ N. *Geophysical Journal International*, *135*(3), 773-789.

Maluski, H., Coulon, C., POPOFF, M. T., & Baudin, P. (1995). 40Ar/39Ar chronology, petrology and geodynamic setting of Mesozoic to early Cenozoic magmatism from the Benue Trough, Nigeria. *Journal of the Geological Society*, *152*(2), 311-326.

Manu-Marfo, D., Aoudia, A., Pachhai, S., & Kherchouche, R. (2019). 3D shear wave velocity model of the crust and uppermost mantle beneath the Tyrrhenian basin and margins. *Scientific reports*, *9*(1), 1-10.

Manya, S., & Maboko, M. A. (2003). Dating basaltic volcanism in the Neoarchaean Sukumaland Greenstone Belt of the Tanzania Craton using the Sm–Nd method: implications for the geological evolution of the Tanzania Craton. *Precambrian Research*, *121*(1-2), 35-45.

McClusky, S., Reilinger, R., Mahmoud, S., Ben Sari, D., & Tealeb, A. (2003). GPS constraints on Africa (Nubia) and Arabia plate motions. *Geophysical Journal International*, *155*(1), 126-138.

McConnell, R. B. (1972). Geological development of the rift system of eastern Africa. *Geological Society of America Bulletin*, *83*(9), 2549-2572.

McCourt, S., & Armstrong, R. A. (1998). SHRIMP U-Pb zircon geochronology of granites from the Central Zone, Limpopo Belt, southern Africa: Implications for the age of the Limpopo Orogeny. *South African Journal of Geology*, *101*(4), 329-338.

Meier, U., Curtis, A., & Trampert, J. (2007). Global crustal thickness from neural network inversion of surface wave data. *Geophysical Journal International*, *169*(2), 706-722.

Milesi, J. P., Frizon de Lamotte, D., de Kock, G., and Toteu, F. (2010). Tectonic Map of Africa, 2nd Edition, Commission for the Geological Map of the World.

Montagner, J. P., Marty, B., Stutzmann, E., Sicilia, D., Cara, M., Pik, R., ... & Debayle, E. (2007). Mantle upwellings and convective instabilities revealed by seismic tomography and helium isotope geochemistry beneath eastern Africa. *Geophysical Research Letters*, *34*(21).

Mooney, W. D., Laske, G., & Masters, T. G. (1998). CRUST 5.1: A global crustal model at 5× 5. *Journal of Geophysical Research: Solid Earth*, *103*(B1), 727-747.

Moschetti, M. P., Ritzwoller, M. H., Lin, F. C., & Yang, Y. (2010). Crustal shear wave velocity structure of the western United States inferred from ambient seismic noise and earthquake data. *Journal of Geophysical Research: Solid Earth*, *115*(B10).

1214 Moulik, P., & Ekström, G. (2014). An anisotropic shear velocity model of the Earth's mantle using normal
1215   modes, body waves, surface waves and long-period waveforms. *Geophysical Journal International*, *199*(3),
1216   1713-1738.

1217 Mulibo, G. D., & Nyblade, A. A. (2013). Mantle transition zone thinning beneath eastern Africa: Evidence for
1218   a whole-mantle superplume structure. *Geophysical Research Letters*, *40*(14), 3562-3566.

1219 Nataf, H. C., & Ricard, Y. (1996). 3SMAC: an a priori tomographic model of the upper mantle based on
1220   geophysical modeling. *Physics of the Earth and Planetary Interiors*, *95*(1-2), 101-122.

1221 Nicollet, C. (1990). Occurrences of grandidierite, serendibite and tourmaline near Ihosy, southern
1222   Madagascar. *Mineralogical Magazine*, *54*(374), 131-133.

1223 Niu, F., & James, D. E. (2002). Fine structure of the lowermost crust beneath the Kaapvaal craton and its
1224   implications for crustal formation and evolution. *Earth and Planetary Science Letters*, 200(1-2), 121-130.

1225 Nocquet, J. M., & Calais, E. (2003). Crustal velocity field of western Europe from permanent GPS array
1226   solutions, 1996–2001. *Geophysical Journal International*, *154*(1), 72-88.

1227 Nyblade, A. A., & Robinson, S. W. (1994). The african superswell. *Geophysical research letters*, *21*(9), 765-
1228   768.

1229 Nyblade, A. A., Owens, T. J., Gurrola, H., Ritsema, J., & Langston, C. A. (2000). Seismic evidence for a deep
1230   upper mantle thermal anomaly beneath east Africa. *Geology*, *28*(7), 599-602.

1231 Nyblade, A., Dirks, P., Durrheim, R., Webb, S., Jones, M., et al. (2008). AfricaArray: Developing a geosciences
1232   workforce for Africa's natural resource sector. *The Leading Edge*, 27(10), 1358-1361.

1233 O'Donnell, J. P., Adams, A., Nyblade, A. A., Mulibo, G. D., & Tugume, F. (2013). The uppermost mantle shear
1234   wave velocity structure of eastern Africa from Rayleigh wave tomography: Constraints on rift
1235   evolution. *Geophysical Journal International*, *194*(2), 961-978.

1236 Ojo, A. O., Ni, S., & Li, Z. (2017). Crustal radial anisotropy beneath Cameroon from ambient noise
1237   tomography. *Tectonophysics*, *696*, 37-51.

1238 Ojo, A. O., Ni, S., Chen, H., & Xie, J. (2018). Crust-mantle coupling mechanism in Cameroon, West Africa,
1239   revealed by 3D S-wave velocity and azimuthal anisotropy. *Physics of the Earth and Planetary*
1240   *Interiors*, *274*, 195-213.

1241 Ojo, A. O., Ni, S., Xie, J., & Zhao, L. (2019). Further constraints on the shear wave velocity structure of
1242   Cameroon from joint inversion of receiver function, Rayleigh wave dispersion and ellipticity
1243   measurements. *Geophysical Journal International*, *217*(1), 589-619.

1244 Owens, T. J., Crotwell, H. P., Groves, C., & Oliver-Paul, P. (2004). SOD: Standing order for data. Seismological
1245   Research Letters, 75(4), 515-520.

1246 Panning, M. P., Lekić, V., & Romanowicz, B. A. (2010). Importance of crustal corrections in the development
1247   of a new global model of radial anisotropy. *Journal of Geophysical Research: Solid Earth*, *115*(B12).

1248 Park, Y., & Nyblade, A. A. (2006). P-wave tomography reveals a westward dipping low velocity zone beneath
1249   the Kenya Rift. *Geophysical Research Letters*, *33*(7).

1250 Pasyanos, M. E., & Nyblade, A. A. (2007). A top to bottom lithospheric study of Africa and
1251   Arabia. *Tectonophysics*, *444*(1-4), 27-44.

1252 Pasyanos, M. E., Masters, T. G., Laske, G., & Ma, Z. (2014). LITHO1. 0: An updated crust and lithospheric
1253   model of the Earth. *Journal of Geophysical Research: Solid Earth*, *119*(3), 2153-2173.

1254 Petters, S. W. (1991). *Regional geology of Africa* (Vol. 722). Berlin-Heidelberg: Springer-Verlag.

1255 Pik, R., Marty, B., & Hilton, D. R. (2006). How many mantle plumes in Africa? The geochemical point of
1256   view. *Chemical Geology*, *226*(3-4), 100-114.

1257 Piqué, A. (1999). The geological evolution of Madagascar: an introduction. *Journal of African Earth*
1258   *Sciences*, *4*(28), 919-930.
1259 Pourpoint, M., Anandakrishnan, S., Ammon, C. J., & Alley, R. B. (2018). Lithospheric structure of Greenland
1260   from ambient noise and earthquake surface wave tomography. *Journal of Geophysical Research: Solid*
1261   *Earth*, *123*(9), 7850-7876.
1262 Pratt, M. J., Wysession, M. E., Aleqabi, G., Wiens, D. A., Nyblade, A. A., Shore, P., ... & Barruol, G. (2017).
1263   Shear velocity structure of the crust and upper mantle of Madagascar derived from surface wave
1264   tomography. *Earth and Planetary Science Letters*, *458*, 405-417.
1265 Priestley, K., McKenzie, D., Debayle, E., & Pilidou, S. (2008). The African upper mantle and its relationship to
1266   tectonics and surface geology. *Geophysical Journal International*, *175*(3), 1108-1126.
1267 Rabinowitz, P. D., Coffin, M. F., & Falvey, D. (1983). The separation of Madagascar and
1268   Africa. *Science*, *220*(4592), 67-69.
1269 Rawlinson, N., & Sambridge, M. (2004). Multiple reflection and transmission phases in complex layered media
1270   using a multistage fast marching method. *Geophysics*, *69*(5), 1338-1350.
1271 Rawlinson, N., & Sambridge, M. (2005). The fast marching method: an effective tool for tomographic imaging
1272   and tracking multiple phases in complex layered media. *Exploration Geophysics*, *36*(4), 341-350.
1273 Rawlinson, N., & Spakman, W. (2016). On the use of sensitivity tests in seismic tomography. *Geophysical*
1274   *Journal International*, *205*(2), 1221-1243.
1275 Rawlinson, N., Hauser, J., & Sambridge, M. (2008). Seismic ray tracing and wavefront tracking in laterally
1276   heterogeneous media. *Advances in Geophysics*, *49*, 203-273.
1277 Rawlinson, N., Kool, M. D., & Sambridge, M. (2006). Seismic wavefront tracking in 3D heterogeneous media:
1278   applications with multiple data classes. *Exploration Geophysics*, *37*(4), 322-330.
1279 Rawlinson, N., Pozgay, S., & Fishwick, S. (2010). Seismic tomography: a window into deep Earth. *Physics of*
1280   *the Earth and Planetary Interiors*, *178*(3-4), 101-135.
1281 Rey, P., Vanderhaeghe, O., & Teyssier, C. (2001). Gravitational collapse of the continental crust: definition,
1282   regimes and modes. *Tectonophysics*, *342*(3-4), 435-449.
1283 Ring, U. (1994). The influence of preexisting structure on the evolution of the Cenozoic Malawi rift (East African
1284   rift system). *Tectonics*, *13*(2), 313-326.
1285 Ritsema, J., & van Heijst, H. (2000). New seismic model of the upper mantle beneath Africa. *Geology*, *28*(1),
1286   63-66.
1287 Ritsema, J., Nyblade, A. A., Owens, T. J., Langston, C. A., & VanDecar, J. C. (1998). Upper mantle seismic
1288   velocity structure beneath Tanzania, east Africa: Implications for the stability of cratonic
1289   lithosphere. *Journal of Geophysical Research: Solid Earth*, *103*(B9), 21201-21213.
1290 Ritsema, J., van Heijst, H. J., & Woodhouse, J. H. (1999). Complex shear wave velocity structure imaged beneath
1291   Africa and Iceland. *Science*, *286*(5446), 1925-1928.
1292 Ritzwoller, M. H., & Levshin, A. L. (1998). Eurasian surface wave tomography: Group velocities. *Journal of*
1293   *Geophysical Research: Solid Earth*, *103*(B3), 4839-4878.
1294 Ritzwoller, M. H., Shapiro, N. M., Barmin, M. P., & Levshin, A. L. (2002). Global surface wave diffraction
1295   tomography. *Journal of Geophysical Research: Solid Earth*, *107*(B12), ESE-4.
1296 Rogers, N., Macdonald, R., Fitton, J. G., George, R., Smith, M., & Barreiro, B. (2000). Two mantle plumes
1297   beneath the East African rift system: Sr, Nd and Pb isotope evidence from Kenya Rift basalts. *Earth and*
1298   *Planetary Science Letters*, *176*(3-4), 387-400.

1299 Rosenbaum, G., & Lister, G. S. (2004). Neogene and Quaternary rollback evolution of the Tyrrhenian Sea, the
1300   Apennines, and the Sicilian Maghrebides. *Tectonics*, *23*(1).

1301 Rozendaal, A., Philander, C., & De Meijer, R. J. (1999). Mineralogy of heavy mineral placers along the west
1302   coast of South Africa. In *Heavy Minerals 1999, Symposium S* (Vol. 23, pp. 63-66).

1303 Rudnick, R. L., & Fountain, D. M. (1995). Nature and composition of the continental crust: a lower crustal
1304   perspective. *Reviews of geophysics*, 33(3), 267-309.

1305 Rudnick, R. L., & Gao, S. (2003). Composition of the continental crust. The crust, 3, 1-64.

1306 Rychert, C. A., & Shearer, P. M. (2009). A global view of the lithosphere-asthenosphere
1307   boundary. *Science*, *324*(5926), 495-498.

1308 Sambridge, M. (1999a). Geophysical inversion with a neighbourhood algorithm—I. Searching a parameter
1309   space. *Geophysical journal international*, *138*(2), 479-494.

1310 Sambridge, M. (1999b). Geophysical inversion with a neighbourhood algorithm—II. Appraising the
1311   ensemble. *Geophysical Journal International*, *138*(3), 727-746.

1312 Schaeffer, A. J., & Lebedev, S. (2013). Global shear speed structure of the upper mantle and transition
1313   zone. *Geophysical Journal International*, *194*(1), 417-449.

1314 Schandelmeier, H., Wipfler, E., Küster, D., Sultan, M., Becker, R., Stern, R. J., & Abdelsalam, M. G. (1994).
1315   Atmur-Delgo suture: A Neoproterozoic oceanic basin extending into the interior of northeast
1316   Africa. *Geology*, *22*(6), 563-566.

1317 Schlüter, T. (1997). Geology of East Africa.

1318 Schulte-Pelkum, V., Mahan, K. H., Shen, W., & Stachnik, J. C. (2017). The distribution and composition of
1319   high-velocity lower crust across the continental US: Comparison of seismic and xenolith data and
1320   implications for lithospheric dynamics and history. *Tectonics*, *36*(8), 1455-1496.

1321 Schulte-Pelkum, V., Monsalve, G., Sheehan, A., Pandey, M. R., Sapkota, S., Bilham, R., & Wu, F. (2005).
1322   Imaging the Indian subcontinent beneath the Himalaya. *Nature*, *435*(7046), 1222-1225.

1323 Sebai, A., Stutzmann, E., Montagner, J. P., Sicilia, D., & Beucler, E. (2006). Anisotropic structure of the African
1324   upper mantle from Rayleigh and Love wave tomography. *Physics of the Earth and Planetary*
1325   *Interiors*, *155*(1-2), 48-62.

1326 Seber, D., Vallvé, M., Sandvol, E., Steer, D., & Barazangi, M. (1997). Middle East tectonics: applications of
1327   geographic information systems (GIS). *GSA today*, *7*(2), 1-6.

1328 Selway, K. (2015). Negligible effect of hydrogen content on plate strength in East Africa. *Nature*
1329   *Geoscience*, *8*(7), 543-546.

1330 Sethian, J. A. (1996). A fast marching level set method for monotonically advancing fronts. *Proceedings of the*
1331   *National Academy of Sciences*, *93*(4), 1591-1595.

1332 Sethian, J. A., & Popovici, A. M. (1999). 3-D traveltime computation using the fast marching
1333   method. *Geophysics*, *64*(2), 516-523.

1334 Shang, C. K., Satir, M., Morteani, G., & Taubald, H. (2010). Zircon and titanite age evidence for coeval
1335   granitization and migmatization of the early Middle and early Late Proterozoic Saharan Metacraton;
1336   example from the central North Sudan basement. *Journal of African Earth Sciences*, *57*(5), 492-524.

1337 Shapiro, N. M., & Campillo, M. (2004). Emergence of broadband Rayleigh waves from correlations of the
1338   ambient seismic noise. *Geophysical Research Letters*, *31*(7).

1339 Shapiro, N. M., & Ritzwoller, M. H. (2002). Monte-Carlo inversion for a global shear-velocity model of the
1340   crust and upper mantle. *Geophysical Journal International*, *151*(1), 88-105.

Shen, W., & Ritzwoller, M. H. (2016). Crustal and uppermost mantle structure beneath the United States. *Journal of Geophysical Research: Solid Earth*, *121*(6), 4306-4342.

Shen, W., Ritzwoller, M. H., & Schulte-Pelkum, V. (2013). A 3-D model of the crust and uppermost mantle beneath the Central and Western US by joint inversion of receiver functions and surface wave dispersion. *Journal of Geophysical Research: Solid Earth*, *118*(1), 262-276.

Simmons, N. A., Forte, A. M., & Grand, S. P. (2007). Thermochemical structure and dynamics of the African superplume. *Geophysical Research Letters*, 34(2).

Simons, F. J., Van Der Hilst, R. D., Montagner, J. P., & Zielhuis, A. (2002). Multimode Rayleigh wave inversion for heterogeneity and azimuthal anisotropy of the Australian upper mantle. *Geophysical Journal International*, *151*(3), 738-754.

Sobh, M., Ebbing, J., Mansi, A. H., Götze, H.-J., Emry, E. L., & Abdelsalam, M. G. (2020). The lithospheric structure of the Saharan Metacraton from 3-D integrated geophysical-petrological modeling. *Journal of Geophysical Research: Solid Earth*, 125, e2019JB018747. https://doi.org/10.1029/2019JB018747

Stankiewicz, J., & de Wit, M. (2013). 3.5 billion years of reshaped Moho, southern Africa. *Tectonophysics*, 609, 675-689.

Storey, M., Mahoney, J. J., Saunders, A. D., Duncan, R. A., Kelley, S. P., & Coffin, M. F. (1995). Timing of hot spot—related volcanism and the breakup of Madagascar and India. *Science*, *267*(5199), 852-855.

Tadjou, J. M., Nouayou, R., Kamguia, J., Kande, H. L., & Manguelle-Dicoum, E. (2009). Gravity Analysis of the Boundary between the Congo Graton and the Pan-African Belt of Cameroon. *Austrian Journal of Earth Sciences*, *102*(1).

Tang, Z., Julià, J., Zahran, H., & Mai, P. M. (2016). The lithospheric shear-wave velocity structure of Saudi Arabia: young volcanism in an old shield. *Tectonophysics*, *680*, 8-27.

Tchameni, R., Mezger, K., Nsifa, N. E., & Pouclet, A. (2001). Crustal origin of Early Proterozoic syenites in the Congo craton (Ntem complex), South Cameroon. *Lithos*, *57*(1), 23-42.

Tedla, G. E., Van Der Meijde, M., Nyblade, A. A., & Van der Meer, F. D. (2011). A crustal thickness map of Africa derived from a global gravity field model using Euler deconvolution. *Geophysical Journal International*, *187*(1), 1-9.

Thomas, R. J. (1989). A tale of two tectonic terranes. *South African Journal of Geology*, *92*(4), 306-321.

Thompson, D. A., Bastow, I. D., Helffrich, G., Kendall, J. M., Wookey, J., Snyder, D. B., & Eaton, D. W. (2010). Precambrian crustal evolution: seismic constraints from the Canadian Shield. *Earth and Planetary Science Letters*, 297(3-4), 655-666.

Thybo, H., Youssof, M., & Artemieva, I. M. (2019). Southern Africa crustal anisotropy reveals coupled crust-mantle evolution for over 2 billion years. *Nature communications*, *10*(1), 1-10.

Tokam, A. P. K., Tabod, C. T., Nyblade, A. A., Julia, J., Wiens, D. A., & Pasyanos, M. E. (2010). Structure of the crust beneath Cameroon, West Africa, from the joint inversion of Rayleigh wave group velocities and receiver functions. *Geophysical Journal International*, *183*(2), 1061-1076.

Torsvik, T. H., Tucker, R. D., Ashwal, L. D., Eide, E. A., Rakotosolofo, N. A., & De Wit, M. J. (1998). Late Cretaceous magmatism in Madagascar: palaeomagnetic evidence for a stationary Marion hotspot. *Earth and Planetary Science Letters*, *164*(1-2), 221-232.

Trampert, J., & Woodhouse, J. H. (1995). Global phase velocity maps of Love and Rayleigh waves between 40 and 150 seconds. *Geophysical Journal International*, *122*(2), 675-690.

1382 Tugume, F., Nyblade, A., & Julià, J. (2012). Moho depths and Poisson's ratios of Precambrian crust in East
1383   Africa: evidence for similarities in Archean and Proterozoic crustal structure. *Earth and Planetary Science*
1384   *Letters*, 355, 73-81.

1385 Tugume, F., Nyblade, A., Julià, J., & van der Meijde, M. (2013). Precambrian crustal structure in Africa and
1386   Arabia: evidence lacking for secular variation. *Tectonophysics*, *609*, 250-266.

1387 Turner, S., Regelous, M., Kelley, S., Hawkesworth, C., & Mantovani, M. (1994). Magmatism and continental
1388   break-up in the South Atlantic: high precision40Ar-39Ar geochronology. *Earth and Planetary Science*
1389   *Letters*, *121*(3-4), 333-348.

1390 Van der Meijde, M., Fadel, I. E. A. M., Ditmar, P., & Hamayun, M. (2015). Uncertainties in crustal thickness
1391   models for data sparse environments: A review for South America and Africa. *Journal of Geodynamics*, *84*,
1392   1-18.

1393 Veevers, J. J., Cole, D. I. & Cowan, E. J. (1994). Southern Africa: Karoo Basin and Cape Fold Belt. In: Veevers,
1394   J. J. & Powell, C. McA. (eds) *Permian Triassic Pangean Basins and Foldbelts along the Panthalassan*
1395   *Margin of Gondwanaland. Geological Society of America, Memoirs* 184, 223-279.

1396 Vergés, J. & Sàbat, F. (1999) Constraints on the western Mediterranean kinematics evolution along a 1,000 -km
1397   transect from Iberia to Africa. In: *The Mediterranean Basins:Tertiary Extension within the Alpine Orogen*
1398   (Ed. by B. Durand, L. Jolivet, F. Horvath & M. Se¤ranne), pp. 63^80, Geol. Soc. Spec. Pub., 156

1399 Wang, T., Gao, S. S., Dai, Y., Yang, Q., & Liu, K. H. (2019). Lithospheric Structure and Evolution of Southern
1400   Africa: Constraints From Joint Inversion of Rayleigh Wave Dispersion and Receiver
1401   Functions. *Geochemistry, Geophysics, Geosystems*, *20*(7), 3311-3327.

1402 Weeraratne, D. S., Forsyth, D. W., Fischer, K. M., & Nyblade, A. A. (2003). Evidence for an upper mantle plume
1403   beneath the Tanzanian craton from Rayleigh wave tomography. *Journal of Geophysical Research: Solid*
1404   *Earth*, *108*(B9).

1405 Welford, J. K., Clowes, R. M., Ellis, R. M., Spence, G. D., Asudeh, I., & Hajnal, Z. (2001). Lithospheric structure
1406   across the craton-Cordilleran transition of northeastern British Columbia. *Canadian Journal of Earth*
1407   *Sciences*, *38*(8), 1169-1189.

1408 Wessel, P., Smith,W. H. F., Scharroo, R., Luis, J., & Wobbe, F. (2013). Generic mapping tools: Improved version
1409   released. *Eos, Transactions American Geophysical Union*, *94*(45), 409–410.
1410   https://doi.org/10.1002/2013EO450001

1411 Williams, M. L., Dumond, G., Mahan, K., Regan, S., & Holland, M. (2014). Garnet-forming reactions in felsic
1412   orthogneiss: Implications for densification and strengthening of the lower continental crust. *Earth and*
1413   *Planetary Science Letters*, *405*, 207-219.

1414 Wilson, M., and R. Guiraud (1992), Magmatism and rifting in Western and Central Africa, from Late Jurassic
1415   to Recent times, Tectonophysics, 213, 203–225.

1416 Wittlinger, G., Farra, V., Hetényi, G., Vergne, J., & Nábělek, J. (2009). Seismic velocities in Southern Tibet
1417   lower crust: a receiver function approach for eclogite detection. *Geophysical Journal International*, *177*(3),
1418   1037-1049.

1419 Wolfenden, E., Ebinger, C., Yirgu, G., Deino, A., & Ayalew, D. (2004). Evolution of the northern Main
1420   Ethiopian rift: birth of a triple junction. *Earth and Planetary Science Letters*, *224*(1-2), 213-228.

1421 Woodhouse, J. H., & Dziewonski, A. M. (1984). Mapping the upper mantle: Three-dimensional modeling of
1422   Earth structure by inversion of seismic waveforms. *Journal of Geophysical Research: Solid Earth*, *89*(B7),
1423   5953-5986.

Xia, Y., & Chen, X. (2020). Observation of a New Long-Period (16-s) Persistent Tremor Originating in the Gulf of Guinea. Geophysical Research Letters, 47(15), e2020GL088137.

Xia, Y., Ni, S., & Zeng, X. (2013). Twin enigmatic microseismic sources in the Gulf of Guinea observed on intercontinental seismic stations. *Geophysical Journal International*, *194*(1), 362-366.

Yang, Y., & Ritzwoller, M. H. (2008). Characteristics of ambient seismic noise as a source for surface wave tomography. *Geochemistry, Geophysics, Geosystems*, *9*(2).

Yang, Y., Ritzwoller, M. H., Levshin, A. L., & Shapiro, N. M. (2007). Ambient noise Rayleigh wave tomography across Europe. *Geophysical Journal International*, *168*(1), 259-274.

Yang, Y., Ritzwoller, M. H., Lin, F. C., Moschetti, M. P., & Shapiro, N. M. (2008a). Structure of the crust and uppermost mantle beneath the western United States revealed by ambient noise and earthquake tomography. *Journal of Geophysical Research: Solid Earth*, *113*(B12).

Yang, Y., Li, A., & Ritzwoller, M. H. (2008b). Crustal and uppermost mantle structure in southern Africa revealed from ambient noise and teleseismic tomography. *Geophysical Journal International*, *174*(1), 235-248.

Yao, H., Beghein, C., & Van Der Hilst, R. D. (2008). Surface wave array tomography in SE Tibet from ambient seismic noise and two-station analysis-II. Crustal and upper-mantle structure. *Geophysical Journal International*, *173*(1), 205-219.

Yao, H., van Der Hilst, R. D., & De Hoop, M. V. (2006). Surface-wave array tomography in SE Tibet from ambient seismic noise and two-station analysis—I. Phase velocity maps. *Geophysical Journal International*, *166*(2), 732-744.

Yao, H., Van Der Hilst, R. D., & Montagner, J. P. (2010). Heterogeneity and anisotropy of the lithosphere of SE Tibet from surface wave array tomography. *Journal of Geophysical Research: Solid Earth*, *115*(B12).

Yao, Z., Mooney, W. D., Zahran, H. M., & Youssef, S. E. H. (2017). Upper mantle velocity structure beneath the Arabian shield from Rayleigh surface wave tomography and its implications. *Journal of Geophysical Research: Solid Earth*, *122*(8), 6552-6568.

Yoshizawa, K., & Ekström, G. (2010). Automated multimode phase speed measurements for high-resolution regional-scale tomography: application to North America. *Geophysical Journal International*, *183*(3), 1538-1558.

Youssof, M., Thybo, H., Artemieva, I. M., & Levander, A. (2013). Moho depth and crustal composition in Southern Africa. *Tectonophysics*, *609*, 267-287.

Zandt, G., Gilbert, H., Owens, T. J., Ducea, M., Saleeby, J., & Jones, C. H. (2004). Active foundering of a continental arc root beneath the southern Sierra Nevada in California. *Nature*, 431(7004), 41-46.

Zeng, X., & Ni, S. (2011). Correction to A persistent localized microseismic source near the Kyushu Island, Japan. *Geophysical Research Letters*, *38*(16).

Zhao, D. (2015). *Multiscale seismic tomography*. Springer.

Zhou, L., Xie, J., Shen, W., Zheng, Y., Yang, Y., Shi, H., & Ritzwoller, M. H. (2012). The structure of the crust and uppermost mantle beneath South China from ambient noise and earthquake tomography. *Geophysical Journal International*, *189*(3), 1565-1583.

Zhou, Y., Nolet, G., Dahlen, F. A., & Laske, G. (2006). Global upper-mantle structure from finite-frequency surface-wave tomography. *Journal of Geophysical Research: Solid Earth*, *111*(B4).